

Algebraic Compression of Free Fermionic Quantum Circuits: Particle Creation, Arbitrary Lattices and Controlled Evolution

Efekan Kökcü ^{1,2,*} Daan Camps ³ Lindsay Bassman Oftelie ¹
Wibe A. de Jong ¹ Roel Van Beeumen ¹ and A. F. Kemper ^{2,†}

¹*Applied Mathematics and Computational Research Division,*

Lawrence Berkeley National Laboratory, Berkeley, CA 94720, USA

²*Department of Physics, North Carolina State University, Raleigh, North Carolina 27695, USA*

³*National Energy Research Scientific Computing Center,*

Lawrence Berkeley National Laboratory, Berkeley, CA 94720, USA

(Dated: May 19, 2025)

Recently we developed a local and constructive algorithm based on Lie algebraic methods for compressing Trotterized evolution under Hamiltonians that can be mapped to free fermions [1, 2]. The compression algorithm yields a circuit which scales linearly in the number of qubits, has a depth independent of evolution time and compresses time-dependent Hamiltonians. The algorithm is limited to simple nearest-neighbor spin interactions and fermionic hopping. In this work, we extend our methods to compress evolution with long-range fermionic hopping, thereby enabling the embedding of arbitrary lattices onto a chain of qubits for fermion models. Moreover, we show that controlled time evolution, as well as fermion creation and annihilation operators can also be compressed. We demonstrate our results by adiabatically preparing the ground state for a half-filled fermionic chain, simulating a 4×4 tight binding model on *ibmq-washington*, and calculating the topological Zak phase on a Quantinuum H1-1 trapped-ion quantum computer. With these new developments, our results enable the simulation of a wider range of models of interest and the efficient compression of subcircuits.

I. INTRODUCTION

Time evolution of a quantum state is one of the potential areas where quantum computers are expected to have an advantage over classical computers; while state preparation lies in the QMA complexity class, time evolution is part of the simpler BQP class. Importantly for applications in physics and chemistry, time evolution is a building block for quantum simulation of physical and chemical systems. It underpins state preparation via adiabatic time evolution, and is a critical step in determining dynamic response functions [3–12]. Furthermore, time evolution under a piecewise constant Hamiltonian has also garnered some recent interest in the context of Floquet dynamics and phase transitions [13–15].

In all cases, a crucial challenge remains: How do we implement the time evolution operator $U(t)$ on a digital quantum computer? The Hamiltonian is typically a sum of Pauli strings σ_k ,

$$\mathcal{H}(t) = \sum_k \alpha_k(t) \sigma_k, \quad (1)$$

where $\alpha_k(t)$ are real functions of time t , and $U(t)$ is related to the Hamiltonian $\mathcal{H}(t)$ via the following equation

$$\partial_t U(t) = -i\mathcal{H}(t)U(t), \quad (2)$$

with initial condition $U(t=0) = \mathcal{I}$. In the simplest case where the Hamiltonian \mathcal{H} is time-independent, this expression simplifies to $U(t) = \exp(-i\mathcal{H}t)$. However, the

Pauli strings σ_k in the Hamiltonian (1) usually do not commute with each other, and thus $U(t)$ cannot be directly decomposed into the 1- and 2-qubit gates that are available on a quantum computer. Finding such a decomposition for $U(t)$ is entitled unitary synthesis and is a difficult problem that generally scales exponentially in the number of qubits [16–18].

A natural choice for decomposition, which covers the time-dependent case as well, is by use of Trotterization, or expansion of the time evolution operator into small time steps δt ,

$$U(t) \approx \underbrace{e^{-i\mathcal{H}(t_1)\delta t} e^{-i\mathcal{H}(t_2)\delta t} \dots e^{-i\mathcal{H}(t_N)\delta t}}_{N \text{ time steps}}, \quad (3)$$

where $t_n = n\delta t$ and $\delta t = t/N$. This has the added advantage that the individual small time steps can be broken up to separate the Pauli strings while limiting the approximation error

$$e^{-i\mathcal{H}(t_n)\delta t} \approx \prod_k e^{-i\alpha_k(t_n)\sigma_k\delta t} + \mathcal{O}(\delta t^2), \quad (4)$$

which leads to a natural circuit implementation. The downside of this approach is that the circuit depth grows with simulation time t , which is undesirable for current era noisy quantum computers which are limited in terms of circuit depths that can be run reliably.

There are a variety of methods proposed to overcome or bypass the problems that arise from the deep circuits from a naïve Trotter implementation. These include variational approaches to learn shorter circuits [19–21], and decompositions based on algebraic methods that do not grow as a function of simulation time [1, 2, 17, 18, 22–24].

* ekokcu@lbl.gov

† akemper@ncsu.edu

In general, due to no-go theorems on fast-forwarding quantum evolution, these circuits may be exponentially deep [25–27]. However, for Hamiltonians that can be mapped onto free fermionic ones, shallow fixed depth circuits, that are independent of simulation time, exist [1, 2, 28–32]. Previous work by the authors and others have demonstrated that the circuit elements that arise from evolution under a *time dependent* 1D nearest-neighbor free fermionic Hamiltonian obey three algebraic properties — fusion, commutation, and turnover — which can be used for an efficient compression algorithm that results in a fixed-depth circuit. While the class of free fermionic Hamiltonians is somewhat restrictive, since it includes some of the more common models studied in quantum computing — such as the nearest-neighbor transverse field Ising model (TFIM) and nearest-neighbor transverse field XY model (TFXY) — the compression algorithm has found applications [10, 33], or has otherwise set a benchmark for what comprises a minimal circuit [24, 34–38]. Since the compression algorithm starts from a Trotter decomposition, it readily handles evolution under a time-dependent Hamiltonian as well. Moreover, the circuit compression is not limited to time evolution, but is applicable to any circuit elements that obey a few key relationships. Thus, the compression algorithm can also be used for subcircuits built of free fermionic operators. This situation arises regularly because part of interacting fermionic evolution is free fermion hopping.

In this paper, we extend our previous compression work in four ways. We show that the evolution under the following can be compressed:

1. long-range fermionic hopping and fermionic swap (FSWAP) operators (Sec. III A),
2. Hermitian linear combinations of particle creation/annihilation operators (Sec. III B),
3. free fermionic evolution controlled by a single ancilla qubit (Sec. IV B),
4. 1D TFIM, TFX, and Kitaev models with periodic boundary conditions (Appendix B).

These developments, when combined, lead to a number of significant improvements and enhanced capabilities of our approach. First, long-range hopping and FSWAP compression enables the compression of free fermionic evolution on any lattice, not just linear chains. Moreover, the FSWAP operator is key in any situation where fermionic statistics matter. Second, compressing single-particle creation operators combines the preparation of a free fermionic or Hartree-Fock state into a subsequent time evolution. And finally, controlled evolution is an important yet difficult problem, and we show that it is possible to compress this type of circuits which have a single control ancilla. The most notable application is the compression of Hadamard-test style circuits, where wave function overlaps need to be measured. If a controlled evolution with multiple ancilla is required, for example

in the construction of a SELECT oracle, our single control compressed evolution circuit can be easily extended to admit multi-controlled evolution by introducing additional ancilla and Toffoli gates [39].

The paper is structured as follows. In Sec. II, we introduce the notations and the gates we will use throughout the paper, as well as the notions of blocks, block rules and compression theorems from Refs. [1, 2]. We then introduce the block mappings from the same papers for TFIM and TFX models, and show their connections to free fermions. In Sec. III A, we show that these TFIM and TFX mappings can be used to compress free fermions on any lattice. We demonstrate this by simulating a 4×4 tight binding model on *ibmq-washington*. In Sec. III B, we introduce a new block mapping which allows us to compress the creation-/annihilation of single fermions as well as fermion pairs. We demonstrate this by preparing the ground state of a TFX model Hamiltonian by using adiabatic state preparation. In Sec. IV A, we introduce a new mathematical structure “ Q -block”, Q -block rules, and a Q -compression which allows us to compress both Q -blocks and blocks together. In Sec. IV B and Sec. IV C, we provide Q -block mappings that allow us to compress controlled evolutions of both free fermions, and free fermions with single fermion creation/annihilation, on any given lattice. We use the Q -block mapping for the free fermions to demonstrate the topological phase transition of the free Creutz-Hubbard model, by calculating ground state overlaps over different parameters in the phase space using Quantinuum’s H1-1E emulator and H1-1 QPU hardware.

The compression software is available as part of the fast free fermion compiler (F3C) [40, 41] at <https://github.com/QuantumComputingLab>. F3C is based on the QCLAB toolbox [42, 43] for creating and representing quantum circuits.

II. NOTATION AND RECAP

In this section, we will define short-hand notations for gates such as “Pauli string rotations” and “free fermionic gates”, and re-state certain theorems and results from our previous works [1, 2] for completeness.

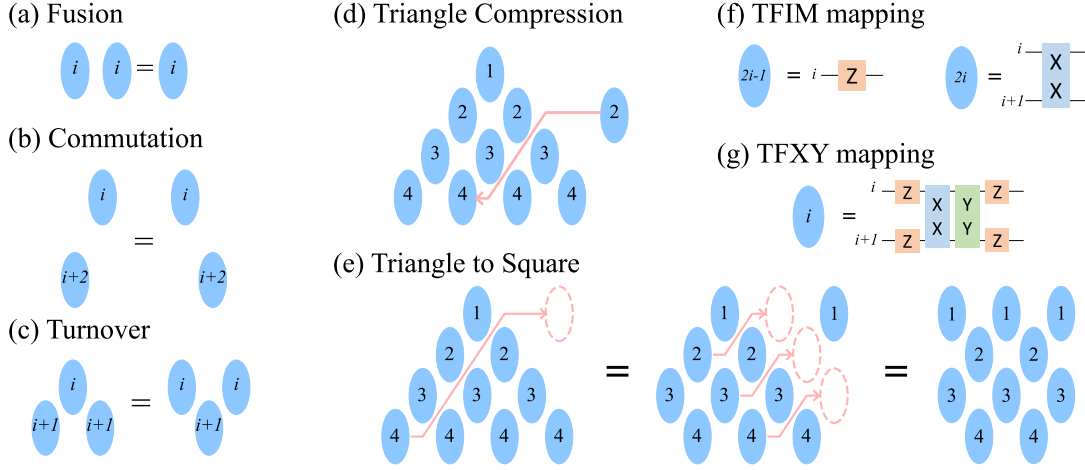


FIG. 1. Summary of the results from Refs. [1, 2] that we will use in this work. Panels (a-c) illustrate the block properties listed in Def. 1. Panel (d) illustrates the triangle structure and how it can absorb a B -block via the B -block properties. Panel (e) is an illustration of the usage of B -block properties to transform a triangle into a shallower square structure. Panels (f) and (g) illustrate two different realizations or representations of the abstract B -block objects as circuit elements, i.e. B -blockmappings, for transverse field Ising model (TFIM) and transverse field XY (TFXY) model. Note that B -blockmappings are not limited to TFIM and TFX, and more examples can be found in Refs. [1, 2].

A. Notation for circuit elements

Throughout this paper, we will illustrate the following 1- and 2-qubit operators as below:

$$\begin{aligned}
 e^{i\theta X_1} &= \begin{array}{c} \text{---} \text{X} \text{---} \\ \theta \end{array} & e^{i\theta X_1 X_2} &= \begin{array}{c} \text{---} \text{X} \text{---} \\ \text{---} \text{X} \text{---} \\ \theta \end{array} \\
 e^{i\theta Y_1} &= \begin{array}{c} \text{---} \text{Y} \text{---} \\ \theta \end{array} & e^{i\theta Y_1 Y_2} &= \begin{array}{c} \text{---} \text{Y} \text{---} \\ \text{---} \text{Y} \text{---} \\ \theta \end{array} \\
 e^{i\theta Z_1} &= \begin{array}{c} \text{---} \text{Z} \text{---} \\ \theta \end{array} & e^{i\theta Z_1 Z_2} &= \begin{array}{c} \text{---} \text{Z} \text{---} \\ \text{---} \text{Z} \text{---} \\ \theta \end{array}
 \end{aligned} \tag{5}$$

In some figures, such as Fig. 1(f) and (g), angles are omitted for convenience. Unless otherwise specified, it is assumed that the angle for each gate is a free parameter in these cases. To extend the notation to generic Pauli strings, we will frequently use gate representations of the forms $e^{i\theta X_1 Z_2 Z_3 \dots Z_{n-1} X_n}$ and $e^{i\theta Y_1 Z_2 Z_3 \dots Z_{n-1} Y_n}$. We illustrate these operators here for $n = 4$:

$$\begin{aligned}
 e^{i\theta X_1 Z_2 Z_3 X_4} &= \begin{array}{c} \text{---} \text{X} \text{---} \\ \text{---} \text{Z} \text{---} \\ \text{---} \text{Z} \text{---} \\ \text{---} \text{X} \text{---} \\ \theta \end{array} & e^{i\theta Y_1 Z_2 Z_3 Y_4} &= \begin{array}{c} \text{---} \text{Y} \text{---} \\ \text{---} \text{Z} \text{---} \\ \text{---} \text{Z} \text{---} \\ \text{---} \text{Y} \text{---} \\ \theta \end{array}
 \end{aligned}$$

Note that these gates correspond to exponentials of single Pauli strings, which can be implemented via 1-qubit gates and CNOT gates [23, 44, 45].

B. Block Definition

In Refs. [1, 2], we introduced a novel mathematical operator referred to as a *block* (B) and characterized by three specific properties. These defining features are succinctly outlined in Definition 1 below. A block is denoted by index i and one or more parameters $\vec{\theta}$, typically expressed as $B_i(\vec{\theta})$. It can be associated with specific parameterized quantum gate operations. Because in this paper another type of block is defined, we refer to the block structure from [1, 2] as B -block.

Definition 1 (B -block [1, 2]). Define a “ B -block” $B_i(\vec{\theta})$ as a structure that satisfies the following three properties:

1. **Fusion:** for any set of parameters $\vec{\alpha}$ and $\vec{\beta}$, there exist \vec{a} such that

$$B_i(\vec{\alpha}) B_i(\vec{\beta}) = B_i(\vec{a}), \tag{6}$$

2. **Commutation:** for any set of parameters $\vec{\alpha}$ and $\vec{\beta}$ such that

$$B_i(\vec{\alpha}) B_j(\vec{\beta}) = B_j(\vec{\beta}) B_i(\vec{\alpha}), \quad |i - j| > 1, \tag{7}$$

3. **Turnover:** for any set of parameters $\vec{\alpha}$, $\vec{\beta}$ and $\vec{\gamma}$ there exist \vec{a} , \vec{b} and \vec{c} such that

$$B_i(\vec{\alpha}) B_{i+1}(\vec{\beta}) B_i(\vec{\gamma}) = B_{i+1}(\vec{a}) B_i(\vec{b}) B_{i+1}(\vec{c}). \tag{8}$$

These three properties are summarized in Fig. 1 panels (a-c). Based on these properties, we have shown in [1, 2] that any quantum circuit that only consist of B -blocks can be compressed to a triangle, also indicated in Fig. 1

panel (d), where the block on the right follows the red line down, using repeated turnover operations, and fuses with the block at the end of the line. Additionally, as shown in panel (e), a triangle can be transformed into a shallower structure, known as a square, using only B-block properties.

C. TFIM and TFX Y Block Mappings

In Refs. [1, 2], we introduced several B -block mappings which map a certain set of gates to a list of B -blocks, including mappings for the 1-D TFIM, TFX Y, Kitaev and XY model. In this paper, we will only be focusing on the TFIM and TFX Y block mappings, which are shown in panels (f-g) of Fig. 1. Mathematically, the TFIM block mapping is given by

$$\begin{aligned} B_{2i-1}^{\text{TFIM}}(\theta) &= e^{i\theta Z_i}, \\ B_{2i}^{\text{TFIM}}(\theta) &= e^{i\theta X_i X_{i+1}}, \end{aligned} \quad (9)$$

where $i > 0$, and the TFX Y block mapping is given by

$$B_i^{\text{TFXY}}(\vec{\theta}) = e^{i\theta_1 Z_i} e^{i\theta_2 Z_{i+1}} e^{i\theta_3 X_i X_{i+1}} e^{i\theta_4 Y_i Y_{i+1}} e^{i\theta_5 Z_i} e^{i\theta_6 Z_{i+1}}. \quad (10)$$

The names TFIM and TFX Y mapping come from the gate sets: the TFIM mapping includes only XX and Z gates, and naturally describes a 1-D TFIM Hamiltonian, and the TFX Y mapping includes all XX , YY and Z gates which allows a 1-D TFX Y model Hamiltonian to be naturally represented by the TFX Y mapping. Due to the frequent use of the TFX Y mapping, we introduce the concept of *free fermionic matchgates* to compactly represent these gates, defined as follows:

$$B_i^{\text{TFXY}}(\vec{\theta}) = \begin{array}{|c|} \hline \text{M} \\ \hline \end{array} = \begin{array}{|c|c|c|c|} \hline \text{Z} & \text{X} & \text{Y} & \text{Z} \\ \hline \theta_1 & \theta_2 & \theta_3 & \theta_4 \\ \hline \text{Z} & \text{X} & \text{Y} & \text{Z} \\ \hline \theta_5 & \theta_6 & \theta_7 & \theta_8 \\ \hline \end{array}. \quad (11)$$

We label these gates with letter “M” in the illustrations, as they are a specific instance of what is known in the literature as “matchgates” [20, 46]. However, matchgates are defined differently in other works [47], which are generalized versions of the gate above. We will refer to the gate defined in Eq. (11) as either a “free fermionic matchgate” or a “free fermionic gate”, interchangeably, since they are equivalent to a combination of nearest-neighbor fermion hopping, pair creation-annihilation, and on-site chemical potentials under a Jordan-Wigner transformation.

It was shown in Ref. [1] that the mappings (9) and (10) obey the B -block properties. These two block mappings are equivalent to each other and can be used interchangeably: TFX Y blocks can be transformed to TFIM blocks and vice versa. For example, a conversion from TFIM to TFX Y can be achieved as follows. Starting from a

TFIM triangle on 2 qubits, we can regroup them into TFX Y blocks with certain angles set to zero:

$$\begin{aligned} \begin{array}{|c|c|c|c|} \hline \text{X} & \text{Z} & \text{X} & \\ \hline \theta_1 & \theta_2 & \theta_3 & \theta_4 \\ \hline \text{Z} & \text{X} & \text{Z} & \text{X} \\ \hline \theta_5 & \theta_6 & \theta_7 & \theta_8 \\ \hline \end{array} &= \begin{array}{|c|c|c|c|} \hline \text{X} & \text{Z} & \text{X} & \\ \hline \theta_1 & \theta_2 & \theta_3 & \theta_4 \\ \hline \text{Z} & \text{X} & \text{Z} & \text{X} \\ \hline \theta_5 & \theta_6 & \theta_7 & \theta_8 \\ \hline \end{array} \\ &= \begin{array}{|c|c|c|c|} \hline \text{Z} & \text{X} & \text{Y} & \text{Z} \\ \hline 0 & \theta_1 & \theta_2 & 0 \\ \hline \text{Z} & \text{X} & \text{Y} & \text{Z} \\ \hline 0 & \theta_3 & \theta_4 & 0 \\ \hline \end{array} \\ &= \begin{array}{|c|c|c|c|} \hline \text{Z} & \text{X} & \text{Y} & \text{Z} \\ \hline \theta'_1 & \theta'_2 & \theta'_3 & \theta'_4 \\ \hline \text{Z} & \text{X} & \text{Y} & \text{Z} \\ \hline \theta'_5 & \theta'_6 & \theta'_7 & \theta'_8 \\ \hline \end{array} \end{aligned} \quad (12)$$

In the final step, we used the TFX Y fusion operation given in [1, Sec. III.D]. This TFIM \rightarrow TFX Y transformation will be used frequently in the following sections. The reverse conversion can be realized in a similar way: a YY -rotation is just an XX -rotation with additional Z -rotations on both qubits, thus,

$$\begin{aligned} \begin{array}{|c|c|c|c|} \hline \text{Z} & \text{X} & \text{Y} & \text{Z} \\ \hline \theta_1 & \theta_2 & \theta_3 & \theta_4 \\ \hline \text{Z} & \text{X} & \text{Y} & \text{Z} \\ \hline \theta_5 & \theta_6 & \theta_7 & \theta_8 \\ \hline \end{array} &= \begin{array}{|c|c|c|c|} \hline \text{Z} & \text{X} & \text{Z} & \text{Z} \\ \hline \theta_1 & \theta_2 & -\pi/4 & \theta_3 \\ \hline \text{Z} & \text{X} & \text{Z} & \text{Z} \\ \hline \theta_5 & \theta_6 & -\pi/4 & \theta_7 \\ \hline \end{array} \\ &= \begin{array}{|c|c|c|c|} \hline \text{X} & \text{Z} & \text{X} & \\ \hline \theta'_1 & \theta'_2 & \theta'_3 & \theta'_4 \\ \hline \text{Z} & \text{X} & \text{Z} & \text{X} \\ \hline \theta'_5 & \theta'_6 & \theta'_7 & \theta'_8 \\ \hline \end{array} \end{aligned} \quad (13)$$

where in the last step we have used algebraic compression of TFIM blocks given in [1, Sec. III.C] to rewrite the series of TFIM blocks as a TFIM triangle.

The two mappings each have their own advantages. The TFX Y mapping only requires 2 CNOTs per block [48] using the following circuit decomposition

$$\begin{array}{|c|} \hline \text{M} \\ \hline \end{array} = \begin{array}{|c|c|c|c|} \hline \text{Z} & \text{X} & \text{Y} & \text{Z} \\ \hline \theta_1 & \theta_2 & \theta_3 & \theta_4 \\ \hline \text{Z} & \text{X} & \text{Y} & \text{Z} \\ \hline \theta_5 & \theta_6 & \theta_7 & \theta_8 \\ \hline \end{array} = \begin{array}{|c|c|c|c|} \hline \text{Z} & \text{X} & \text{X} & \text{Z} \\ \hline \theta_1 & -\pi/4 & \theta_3 & \pi/4 \\ \hline \text{Z} & \text{X} & \text{X} & \text{Z} \\ \hline \theta_5 & -\pi/4 & \theta_7 & \pi/4 \\ \hline \end{array}, \quad (14)$$

while the same structure in a TFIM mapping requires 4 CNOTs in general (see Eq. 13), since each XX rotation requires 2 CNOTs. The TFX Y mapping thus only requires half as many CNOTs. On the other hand, compressing a TFIM mapping is approximately 20 times faster on a classical computer and more straightforward [2]. Throughout the paper, we will be using both of these mappings extensively, and benefit from the simplicity of TFIM in proofs, and CNOT efficiency of TFX Y in the circuit constructions and hardware demonstrations.

As shown in [1], the TFIM and TFX Y models are connected to free fermions via the Jordan-Wigner transfor-

mation,

$$\begin{aligned} c_n &= \frac{1}{2} Z_1 Z_2 \cdots Z_{n-1} (X_n - iY_n), \\ c_n^\dagger &= \frac{1}{2} Z_1 Z_2 \cdots Z_{n-1} (X_n + iY_n), \end{aligned} \quad (15)$$

where c_n (resp. c_n^\dagger) are the usual fermionic annihilation (resp. creation) operators. Then, for example, we have

$$\begin{aligned} c_n^\dagger c_{n+1} + \text{H.c.} &= -\frac{1}{2} (X_n X_{n+1} + Y_n Y_{n+1}), \\ c_n^\dagger c_n &= -\frac{1}{2} (I - Z_n), \end{aligned} \quad (16)$$

which can directly be represented by TFIM and TFX Y block mappings. In a similar way, $X_n X_{n+1}$, $Y_n X_{n+1}$, $X_n Y_{n+1}$, and $Y_n Y_{n+1}$ can be written as a linear combination of $c_n^{(\dagger)} c_{n+1}^{(\dagger)}$ terms. With this, we have shown that the TFIM and TFX Y block mappings can be used to compress time evolution circuit for any time dependent, free fermionic Hamiltonian on a 1D open chain with nearest-neighbor hopping $c_{i+1}^\dagger c_i$, nearest-neighbor pair creation (annihilation) $c_{i+1} c_i$ ($c_{i+1}^\dagger c_i^\dagger$), and onsite potential $c_i^\dagger c_i$ terms:

$$\mathcal{H}(t) = \sum_{i=1}^{n-1} (h_i(t) c_i^\dagger c_{i+1} + p_i(t) c_i c_{i+1} + u_i(t) c_i^\dagger c_i) + \text{H.c.} \quad (17)$$

III. NEW BLOCK MAPPING RESULTS

In this section, we will show new results that we obtained with the already existing B -block mappings. First, we will show that the TFX Y and TFIM mappings are capable of representing long range free fermion hoppings as well, and apply this to a 2-D 4×4 tight binding model. Secondly, we show that with the addition of one more element, the TFIM mapping is capable of implementing fermion creation-annihilation as well. With the results of this section, we are now capable of compressing Hamiltonians that have quadratic and linear terms of c_i and c_i^\dagger , which are of the following form:

$$\mathcal{H}(t) = \sum_{i,j} (h_{ij}(t) c_i^\dagger c_j + p_{ij}(t) c_i c_j + \mathbf{q}_i(t) \cdot \mathbf{c}_i) + \text{H.c.}, \quad (18)$$

where long range and creation terms highlighted in bold are new.

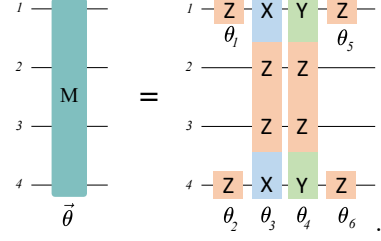
A. Fermionic Swap Gate and Long-Range Hoppings

First, we show that the TFX Y and TFIM block mappings can compress any free fermionic Hamiltonian with

long-range hoppings,

$$\mathcal{H}(t) = \sum_{i,j} (h_{ij}(t) c_i^\dagger c_j + p_{ij}(t) c_i c_j) + \text{H.c.}, \quad (19)$$

where the novelty is the arbitrary lattice connectivity between any i, j pair as highlighted by the boldface \mathbf{j} . To illustrate these long range terms, we define the following generalization of the free fermionic matchgates given in Eq. (11):



$$\vec{\theta} = \theta_1, \theta_2, \theta_3, \theta_4, \theta_5, \theta_6. \quad (20)$$

The above is an illustration of the gate between qubits 1 and 4, however it can be generalized to any pair of qubits. These gates are equivalent to exponentials of linear combinations of Jordan-Wigner transformed versions of long range fermion hopping ($c_1^\dagger c_4, c_4^\dagger c_1$), pair creation-annihilations ($c_1^\dagger c_4^\dagger, c_4 c_1$), and on site chemical potentials ($c_1^\dagger c_1, c_4^\dagger c_4$), i.e.,

$$e^{i(zc_1^\dagger c_4 + z^* c_4^\dagger c_1 + wc_1^\dagger c_4^\dagger + w^* c_4 c_1 + \alpha c_1^\dagger c_1 + \beta c_4^\dagger c_4)}, \quad (21)$$

where $z, w \in \mathbb{C}$ complex numbers, and $\alpha, \beta \in \mathbb{R}$ real numbers. The Z chain between the end qubits 1 and 4 results from the Z chain given in the Jordan-Wigner transformation given in Eq. (15).

In order to show that time evolution under the long range free fermionic Hamiltonian given in Eq. (24), we will use the fermionic swap (FSWAP) gate, which is defined as follows

$$\mathcal{F}_{j,j+1} = i \begin{bmatrix} 1 & 0 & 0 & 0 \\ 0 & 0 & 1 & 0 \\ 0 & 1 & 0 & 0 \\ 0 & 0 & 0 & -1 \end{bmatrix}, \quad (22)$$

for nearest neighbor qubits j and $j+1$. Up to a global phase i , this operation is equivalent to a swap operation that keeps track of the sign generated by fermion exchange, which leads to the following relations

$$\begin{aligned} \mathcal{F}_{i,i+1} c_i^{(\dagger)} \mathcal{F}_{i,i+1}^\dagger &= c_{i+1}^{(\dagger)}, \\ \mathcal{F}_{i,i+1} c_{i+1}^{(\dagger)} \mathcal{F}_{i,i+1}^\dagger &= c_i^{(\dagger)}. \end{aligned} \quad (23)$$

With the global phase i , $\mathcal{F}_{j,j+1}$ can be mapped to a TFX Y block (10) with index j , and parameters $\theta_1 = \theta_2 = 0$ and $\theta_3 = \theta_4 = \theta_5 = \theta_6 = \pi/4$. It follows that the $\mathcal{F}_{j,j+1}$ operation can thus be compressed within the existing TFX Y B -block compression algorithm.

From Eq. (23), we can use FSWAP gates to generate long-range quadratic terms from nearest-neighbor terms,

$$c_1^{(\dagger)} c_4^{(\dagger)} = \mathcal{F}_{3,4} \mathcal{F}_{2,3} c_1^{(\dagger)} c_2^{(\dagger)} \mathcal{F}_{2,3}^\dagger \mathcal{F}_{3,4}^\dagger. \quad (24)$$

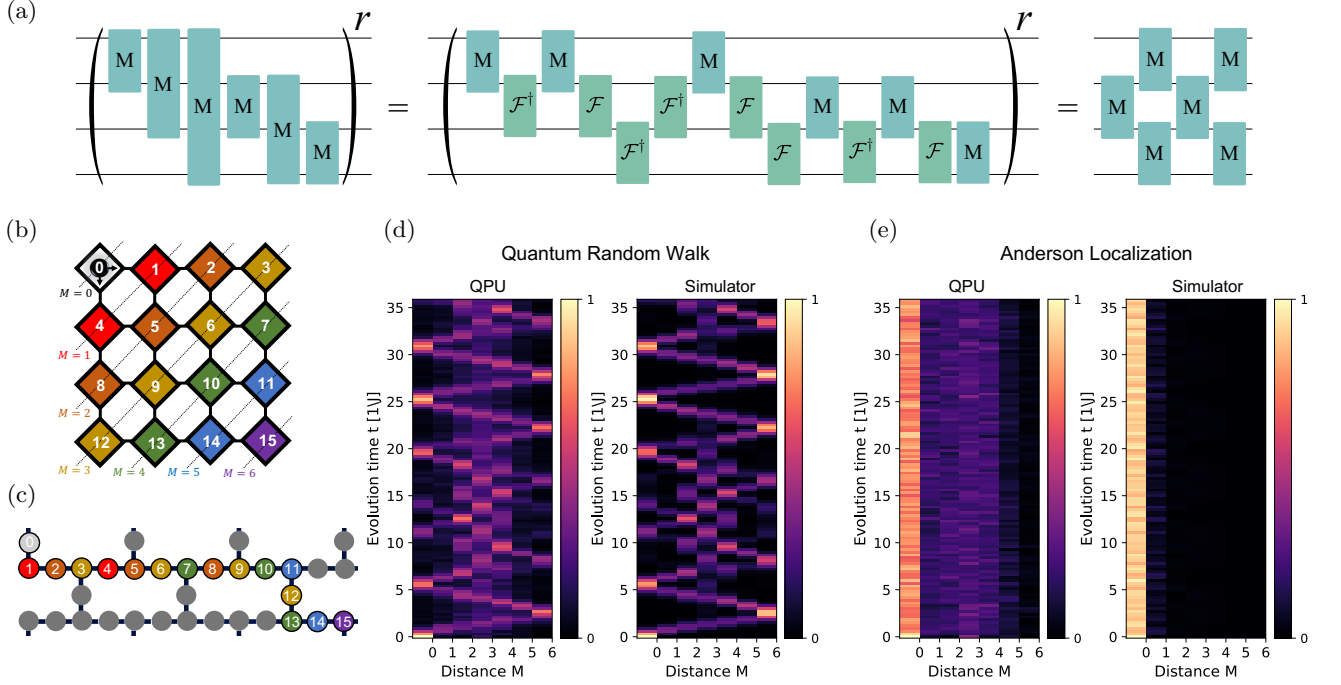


FIG. 2. (a) An illustration of compression of long range hoppings. Any non-local fermion hopping can be written in terms of nearest neighbor hoppings as shown in Eq. (25), which then can be compressed into a TFXY square. The other panels illustrate the simulation results from *ibmq_washington* of a free-fermion on a two-dimensional (2D) lattice. Specifically: (b) Schematic of the 16-site, 2D lattice, color-coded by the distance M each lattice site is from the reference lattice site, labeled ‘0’. The fermion is initialized at reference lattice site ‘0’, and is allowed to evolve freely in time. (c) The topology of the qubits in the *ibmq_washington* quantum processing unit (QPU) is shown, along with how the lattice sites from the schematic in panel (b) are mapped to the particular 16 qubits used in these simulations. (d) The occupation number at each distance M versus time with no disorder in the lattice. This leads to ballistic transport of the fermion. The left-hand plot shows results from the QPU, while the right-hand plot shows results from a noise-free quantum simulator. (e) The occupation number at each distance M versus time with random disorder in the lattice. This leads to Anderson localization of the fermion. The left-hand plot shows results from the QPU, while the right-hand plot shows results from a noise-free quantum simulator.

This expression is an exponent of a long range free fermionic gate, thus we can illustrate Eq. (24) as follows

$$\begin{array}{c} \text{---} \\ | \\ \text{M} \\ | \\ \text{---} \\ \bar{\theta} \end{array} = \begin{array}{c} \text{---} \\ | \\ \text{F}^\dagger \\ | \\ \text{F}^\dagger \end{array} \begin{array}{c} \text{---} \\ | \\ \text{F} \\ | \\ \text{F} \end{array} \begin{array}{c} \text{---} \\ | \\ \text{M} \\ | \\ \text{---} \\ \bar{\theta} \end{array} \quad (25)$$

Here we illustrated fermionic swap (dagger) gates as free fermionic gates with label $\mathcal{F}^{(\dagger)}$, and with a different color to specify them. This way we can decompose a long range hopping into a series of nearest neighbor free fermionic matchgates, i.e. TFXY B -blocks. This means that the TFIM and TFXY block mappings given in Eqs. (9) and (10) can generate long-range quadratic terms, and thus can be used to compress quadratic fermionic Hamiltonians on any lattice. An illustration of this approach is shown in Fig. 2(a), where we schematically decompose and compress r long-range fermionic hoppings.

We utilize our long range free fermion compression to simulate transport of free-fermions on a 2D lattice

on *ibmq_washington* [49]. In particular, we consider a fermion initialized on a reference lattice site, and observe how it evolves. The lattice, pictured in Fig. 2(b), comprises 16 sites with open boundary conditions. The lattice site labeled ‘0’ is considered our reference site, where the fermion is initialized. The lattice sites are color-coded by their taxicab or Manhattan distance M to the reference site. Each lattice site is mapped to a qubit on the *ibmq_washington* quantum processing unit (QPU), which is an IBM Quantum Eagle r1 processor. Note that the 2D lattice of sites is mapped to a one-dimensional chain of qubits on the QPU, and thus requires long-range hopping operations as in Eq. (25). For example, in the 2D lattice, the fermion can hop between nearest-neighbor sites 11 and 15 (see Fig. 2(b)), but when the lattice is mapped to the qubits in the QPU, sites 11 and 15 are no longer neighbors (see Fig. 2(c)), and thus a long-range interaction between these qubits must be implemented.

We examine transport of a fermion on this 16-site lattice both with and without disorder. To do this, we track the occupation number at varying distances M from the reference site as the fermion evolves freely through time.

When there is no disorder in the system, we expect the fermion to behave ballistically and oscillate back and forth within the lattice. Fig. 2(d) shows results from simulating a free fermion on a 2D lattice with no disorder on the *ibmq-washington* QPU as well as on a noise-free quantum simulator. The colors in the plots correspond to the occupation number at each distance M versus evolution time. When there is large random disorder in the system, we expect the fermion to exhibit Anderson localization [50, 51]. Fig. 2(e) shows results from simulating a free fermion on a 2D lattice with large random disorder on the *ibmq-washington* QPU as well as on a noise-free quantum simulator. Simulations on the QPU were performed with 50,000 shots and any shot that did not conserve particle number was discarded. Two straightforward error mitigation techniques were also used to reduce noise in the results from the QPU. The first was a scalable readout error mitigation method implemented with the *mthree* package [52], which reduces errors in quantum measurement via calibration. The second was dynamical decoupling [53–56], a method that can suppress qubit decoherence via the application of a set of pulses (which together amount to application of the identity operator) to idling qubits which cancels the system-environment interaction [57].

While the results from the QPU still exhibit some level of noise, there is good qualitative agreement with the results from the exact simulator, and a difference in transport can clearly be identified between lattices with and without disorder. We attribute the impressive results of these 16-qubit dynamic simulations on a real QPU to our compression algorithm, which produces short-depth circuits that do not grow with increasing evolution time.

B. Fermion Annihilation and Creation

In this section, we demonstrate that the preparation of a product state of any number of free fermionic states can be compressed. Consider the following Hamiltonian:

$$\mathcal{H}(t) = \sum_{i,j} (h_{ij}(t) c_i^\dagger c_j + p_{ij}(t) c_i c_j) + \text{H.c.} + \sum_i (\mathbf{q}_i(t) c_i + \mathbf{q}_i(t)^* c_i^\dagger), \quad (26)$$

where $h_{ij}(t)$, $p_{ij}(t)$ and $q_i(t)$ are complex functions of time. The difference between this Hamiltonian and Eq. (19) is the presence of the lone operators c_i and c_i^\dagger , which are highlighted in bold, and annihilate (resp. create) fermions on site i . These terms cannot be represented by the standard TFIM and TFX mappings from Eqs. (9) and (10).

The evolution under the Hamiltonian given in Eq. (26) yields full control over the particle content of a fermionic state, and allows us to generate any fermionic Gaussian state, i.e. fermion product state [58, 59]. The pair creation terms $c_i c_j$ allow us to change the particle number

by 2, and a repeated application of them leads to a change of particle count by an even number. The addition of c_i terms allows us to change the particle content by an odd number as well, giving us full control. In fact, using the quadratic terms $c_i^{(\dagger)} c_j^{(\dagger)}$ as basis change and Bogolyubov transformations, by $c_i^{(\dagger)}$, we can change the particle content in any given basis, and add/subtract as many particles as desired in a unitary fashion. In Appendix A, we show how to use the evolution under the Hamiltonian Eq. (26) to add/subtract fermions in the momentum basis.

To compress the time evolution of Eq. (26), we extend the TFIM mapping as follows:

$$\begin{aligned} B_1^{\text{CTFIM}}(\theta) &= e^{i\theta X_1} \\ B_{2i}^{\text{CTFIM}}(\theta) &= e^{i\theta Z_i}, \\ B_{2i+1}^{\text{CTFIM}}(\theta) &= e^{i\theta X_i X_{i+1}}, \end{aligned} \quad (27)$$

where the superscript CTFIM is short for creation TFIM, indicating that this mapping contains creation and annihilation of free fermions, and implements free fermions via TFIM terms. An illustration of this mapping is given in Fig. 3(a). Note that this mapping is the same as the TFIM block mapping given in Eq. (9) with the addition of B_1^{CTFIM} and a shift of block indices, i.e. $B_{i+1}^{\text{CTFIM}} = B_i^{\text{TFIM}}$ for $i = 1, 2, 3, \dots$. We will show that this mapping covers all interaction terms in Eq. (26), and that they satisfy the B -block rules given in Def. 1.

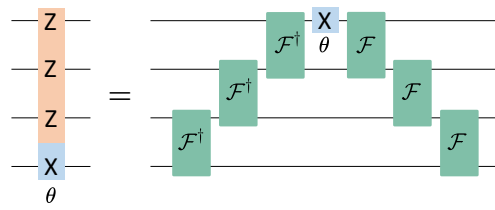
The set of gates given in Eq. (27) enables us to implement all the terms of the Hamiltonian given in Eq. (26). The operator in the exponent of the new block B_1^{CTFIM} is $X_1 \equiv c_1 + c_1^\dagger$. Together with $B_2^{\text{CTFIM}}(\theta) = e^{i\theta Z_1}$, this new term enables this mapping to cover any Hermitian linear combination of c_1 and c_1^\dagger via the following

$$\begin{aligned} B_2^{\text{CTFIM}}(\theta) X_1 B_2^{\text{CTFIM}}(-\theta) &= \cos 2\theta X_1 + \sin 2\theta Y_1 \\ &= e^{2i\theta} c_1 + e^{-2i\theta} c_1^\dagger. \end{aligned} \quad (28)$$

Thus, the $c_1^{(\dagger)}$ term in the Hamiltonian (26) for any complex function of time $q_1(t)$ can be written via the mapping given in Eq. (27). Using the fermionic swap gates, which are part of the TFIM mapping as shown previously, we can move the $c_1^{(\dagger)}$ term around to generate any $c_i^{(\dagger)}$ term for any function $q_i(t)$ by using Eq. (23). For example, $c_4^{(\dagger)}$ can be written in terms of $c_1^{(\dagger)}$ and fermionic swap operators as,

$$c_4^{(\dagger)} = \mathcal{F}_{3,4} \mathcal{F}_{2,3} \mathcal{F}_{1,2} c_1^{(\dagger)} \mathcal{F}_{1,2}^\dagger \mathcal{F}_{2,3}^\dagger \mathcal{F}_{3,4}^\dagger, \quad (29)$$

which we illustrate as,



$$\theta \quad (30)$$

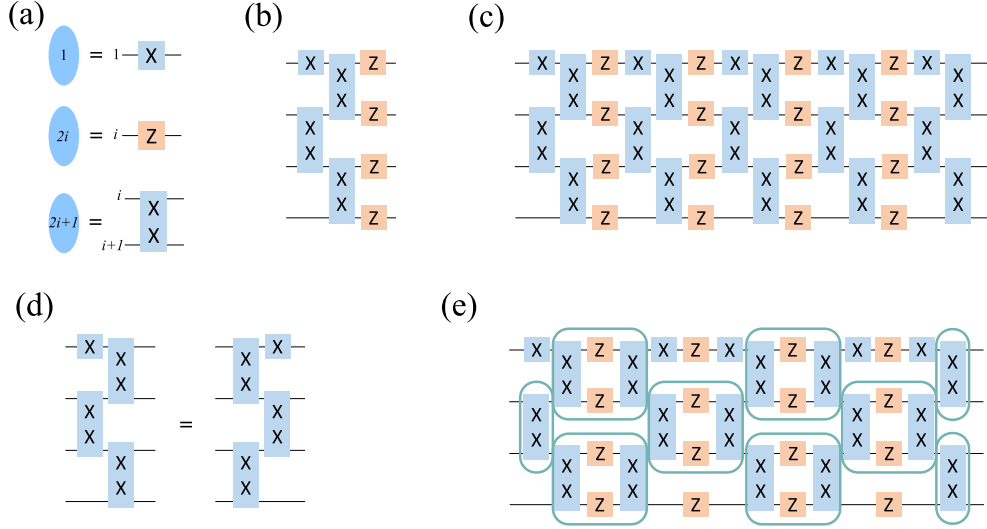


FIG. 3. In panel (a), we show the block mapping that covers the free fermions with creation. By using these, we can build fermionic swaps, and carry the creation-annihilation operator on the first qubit to any other qubit. Panel (b) show the complete set of blocks for 4 qubits. In panel (c), we show the final circuit representing the square structure with this particular block mapping, that can be obtained by using the compression theorems. In this form, the circuit requires $2(n-1)(n+1) = 2(n^2-1) = O(2n^2)$ CNOT gates. By using the relation given in panel (d) on every other $X-XX$ vertical stripe, certain XX gates can be grouped as shown in panel (e). Then using the relation Eq. (12), these groups can be transformed into free fermionic gates. After this simplification, the number CNOTs is reduced to $(n-1)(n+2) = O(n^2)$, which is approximately half of the CNOT count of the circuit in panel (c).

On the left hand side representing $c_4^{(\dagger)}$, we have a rotation generated via Pauli X_4 with a Z -tail due to the Jordan-Wigner transformation (15).

The mapping in Eq. (27) satisfies all B -block rules given in Def. 1. We already know that $\{B_i^{\text{CTFIM}}, i \geq 2\}$ is a B -block mapping, thus we only need to check if the B_1^{CTFIM} satisfies fusion, commutation and turnover rules. Fusion is satisfied since we have

$$B_1^{\text{CTFIM}}(\alpha)B_1^{\text{TFIM}}(\beta) = B_1^{\text{CTFIM}}(\alpha + \beta). \quad (31)$$

Commutation with B_i^{CTFIM} for $i > 3$ is trivially satisfied since they do not share any qubits, and it commutes with B_3^{CTFIM} since X_1 commutes with X_1X_2 even though they both act on qubit 1. Finally, the turnover property is satisfied directly because of the following: the operators in the exponents of B_1^{CTFIM} and B_2^{CTFIM} , i.e., X_1 and Y_1 , form the following representation of $\mathfrak{su}(2)$:

$$\mathfrak{su}(2) \equiv \text{ispan}\{X_1, Z_1, Y_1\}. \quad (32)$$

The Euler decomposition of this representation yields that there exist $a, b, c \in \mathbb{R}$ for any $\alpha, \beta, \gamma \in \mathbb{R}$ such that

$$e^{iaX_1}e^{ibZ_1}e^{icX_1} = e^{i\alpha Z_1}e^{i\beta X_1}e^{i\gamma Z_1}, \quad (33)$$

which is equivalent to

$$\begin{aligned} B_1^{\text{CTFIM}}(a)B_2^{\text{CTFIM}}(b)B_1^{\text{CTFIM}}(c) \\ = B_2^{\text{CTFIM}}(\alpha)B_1^{\text{CTFIM}}(\beta)B_2^{\text{CTFIM}}(\gamma), \end{aligned} \quad (34)$$

where the corresponding angles can be calculated via [1, Eqs. (29) and (30)]. Thus, B_1^{CTFIM} satisfy the turnover

property as well, and the mapping Eq. (27) is a B -block mapping.

This new mapping enables compression of single particle creation/annihilation together with pair creation/annihilation and fermion hoppings. Using the compression theorem for B -blocks, the fixed depth circuits for evolution under the Hamiltonian Eq. (26) are given in Fig. 3. Panel (a) illustrates the CTFIM mapping given in Eq. (27), where we have blocks on the left hand side, and gates on the right hand side. In panel (b), we illustrate a full list of blocks for $n = 4$ qubits. As it can be seen, there are $2n = 8$ blocks. In panel (c), we show the circuit obtained from the square structure (see [1, 2] and Fig. 1(e)) by using the block mapping given in panel (a). In this form, the circuit contains $(n+1)(n-1) = n^2 - 1$ XX gates, which yields $2n^2 - 2$ CNOTs. This CNOT count can be reduced by moving X_1 and X_iX_{i+1} gates around as shown in panel (d). This way, certain XX gates can be brought and grouped together as shown in panel (e). These groups then form TFIM triangles, and can be transformed into a TFX block or a free fermionic gate by Eq. (12). In this way, each group will cost only 2 CNOTs rather than 4. In total, the final CNOT count of the circuit given in panel (e) turns out to be $(n-1)(n+2)$, which is approximately half of the CNOT count of the circuit in panel (c).

We will use an adiabatic state preparation example to demonstrate the compression of free fermions with creation and annihilation. We will be generating the ground

state of the following Hamiltonian

$$\mathcal{H}_0 = -\tilde{t} \sum_{i=1}^{n-1} (c_i^\dagger c_{i+1} + c_{i+1}^\dagger c_i) - \mu \sum_{i=1}^n c_i^\dagger c_i, \quad (35)$$

for $\tilde{t} = 1$ and $\mu = 0$. For large negative values of μ , the chemical potential term will dominate and the ground state will be the empty state $|000\dots 0\rangle$, which is easy to prepare. Thus, if we change μ sufficiently slowly, by the adiabatic theorem we can prepare the ground state of the Hamiltonian with $\mu = 0$ as long as the energy gap between the ground state and the first excited state does not become zero. This method is called adiabatic state preparation (ASP).

ASP comes with competing challenges for the current noisy hardware. First, the Hamiltonian needs to be changed adiabatically — requiring a small $d\mu/dt$ and a long evolution time T . At the same time, due to the Trotter decomposition, the time step δt should be small. Altogether, this leads to a large number of Trotter steps $r = T/\delta t \gg 1$. For the non-compressible cases, it is difficult to simulate $r \gg 1$ due to hardware noise.

A second challenge to adiabatically prepare the ground state of \mathcal{H}_0 stems from the symmetries of the Hamiltonian. The Hamiltonian (35) conserves particle number, which makes the adiabatic state preparation approach difficult. When $\mu = 0$ the Hamiltonian (35) is particle-hole symmetric, and the ground state will be half filled. However, the initial state has no particles in it. Thus, without a symmetry breaking term, it is not possible to reach the ground state of $\mathcal{H}_0(\mu = 0)$ since evolution under Eq. (35) does not change the particle number. More generally, the system has protected level crossings in the spectrum which makes the adiabatic state preparation impossible, unless an additional symmetry breaking term is added to the Hamiltonian to open gaps at those level crossing points.

In the TFX model (which is equivalent to Eq. (35) after a Jordan-Wigner transformation), a global transverse X -direction magnetic field can generate gaps in the spectrum [60]. A global magnetic field is however not compressible; a field on the second site ($X_2 = Z_1(c_2 + c_2^\dagger)$) is cubic in fermion terms, which makes the dynamical Lie algebra grow exponentially with the system size. However, as we have shown, a field on the first site ($c_1 + c_1^\dagger = X_1$) is compressible. Thus, we will add a single term that creates/annihilates particles on site 1,

$$\mathcal{H}'(t) = \lambda(t)(c_1 + c_1^\dagger), \quad (36)$$

which in spin language corresponds to a local magnetic field in X direction. This is sufficient to generate gaps between the ground state and the first excited state. Thus, the addition of \mathcal{H}' addresses both challenges listed above: it opens up gaps by breaking the particle conservation symmetry, and its evolution together with $\mathcal{H}_0(\mu)$ is compressible into a circuit that is independent of the number of Trotter steps r which needs to be large for ASP.

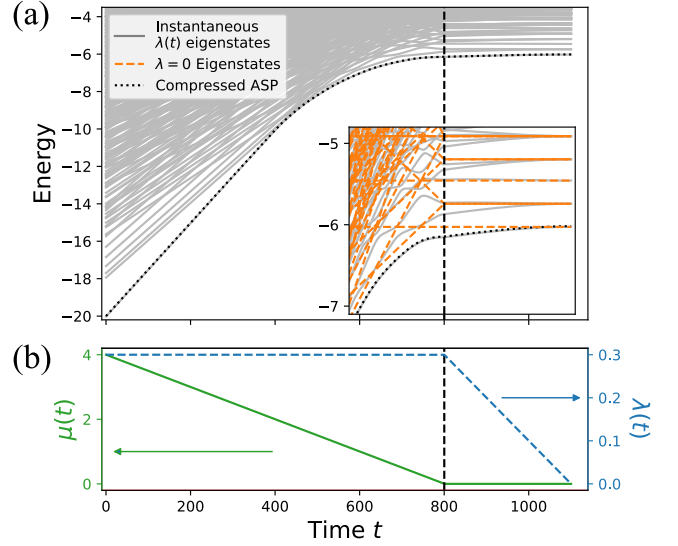


FIG. 4. Numerical results for the adiabatic state preparation for the 1D chain via fermionic compression. (a) Instantaneous eigenstates and the result of the compressed time evolution with the parameters discussed in the text. Inset: a close-up view near the end of the evolution, with the instantaneous eigenvalues of \mathcal{H}_0 (orange dashed lines) and $\mathcal{H} = \mathcal{H}_0 + \mathcal{H}'$ (gray lines). (b) Time evolution of the chemical potential $\mu(t)$ and symmetry-breaking field $\lambda(t)$.

Fig. 4 shows the numerical results of adiabatic state preparation of the ground state of \mathcal{H}_0 for $n = 10$ sites via state vector simulation. We initiate our state with no particles $|\psi(t=0)\rangle = |000\dots 0\rangle$ with $\lambda(t=0) = 0.3$ and $\mu(t=0) = -4$. The amplitude of the chemical potential is large enough to ensure that the 0-particle state has large overlap with the ground state, even with non-zero λ . We evolve the state with $d\mu/dt = -0.005$ and constant $\lambda = 0.3$ to keep the gaps open until we reach $\mu(t) = 0$ at $t = 800$. As a final step, we slowly turn off λ with $d\lambda/dt = -0.001$ and $\mu = 0$ until we reach $\lambda = 0$ to obtain the true ground state of \mathcal{H}_0 in Eq. (35) at $\mu = 0$.

As can be seen in Fig. 4, the energies obtained through adiabatic evolution compare well to the instantaneous ground state energies of $\mathcal{H} = \mathcal{H}_0 + \mathcal{H}'$ with $\lambda = 0.3$. In the inset, it is clear that the ground and the first excited state \mathcal{H}_0 cross frequently — this is due to particle number conservation of \mathcal{H}_0 . The nonzero λ breaks the symmetry and opens up a gap at each of these level crossings between the ground and the first excited states. However, the gap is relatively small, therefore rate of change of μ must be small.

Satisfying the requirements of slow changes in the Hamiltonian, small δt , and a symmetry breaking field is enabled by the compression algorithm, which allows for arbitrarily long evolution at a fixed depth. Thus, both δt and $d\mu/dt$ can be as small as desired in the Trotter expansion. As a simple first order Trotter circuit without compression, using $\delta t = 0.4$ until $t = 800$ and $\delta t = 0.2$ for

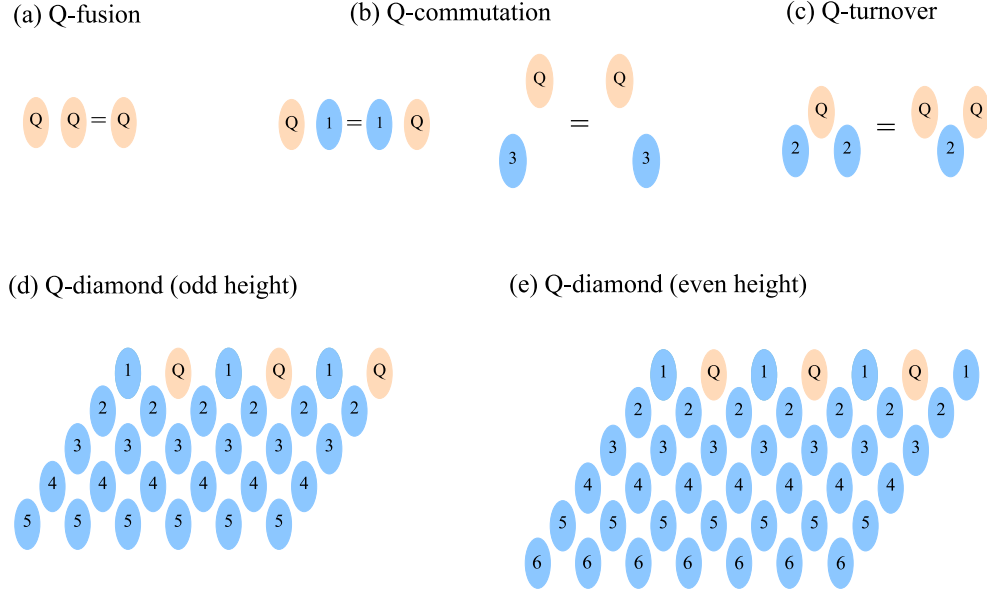


FIG. 5. (a-c) Q -block properties given in Def. 2. (d-e) The diamond structure defined in Def. 3 with heights $n = 5$ and $n = 6$. Notice that the alternating nature of B_1 and Q in the diamond makes the top right corner of the odd height and even height diamonds differ from each other. This leads to different compression sequences for even-odd height diamonds.

the remainder, this circuit consists of 3500 Trotter steps and 315,000 CNOTs. After compression, the circuit is structured as shown in Fig. 3 with only 108 CNOTs.

IV. NEW TYPE OF BLOCK: Q -BLOCK

In this section, we introduce a new type of block, Q -block, which interacts with the blocks via Q -block rules. In the end, the usage of Q -block together with B -blocks will allow us to compress a singly controlled free fermionic evolution with the following Hamiltonian

$$\begin{aligned} \mathcal{H}(t) = & \sum_{i,j} (h_{ij}(t) c_i^\dagger c_j + p_{ij}(t) c_i c_j + q_i(t) c_i) \\ & + \mathbf{Z}_0 \sum_{i,j} (\mathbf{h}'_{ij}(\mathbf{t}) \mathbf{c}_i^\dagger \mathbf{c}_j + \mathbf{p}'_{ij}(\mathbf{t}) \mathbf{c}_i \mathbf{c}_j + \mathbf{q}'_i(\mathbf{t}) \mathbf{c}_i) + \text{H.c.}, \end{aligned} \quad (37)$$

where the 0-th qubit is the control qubit. We also show that 1-D spin models TFX and TFIM with periodic boundary condition are equivalent to singly controlled free fermions, and provide Q -block mappings for these models as well. Finally, we apply our method to calculate the Zak phase of the free Creutz-Hubbard model by calculating the overlap of the ground states of the Creutz-Hubbard model with different parameters that are generated via adiabatic state preparation.

A. Q -block and Q -compression

We define a Q -block as a mathematical operator that satisfies the following three relations.

Definition 2 (Q -block). *Given B -blocks B_i with $i \geq 1$, define a Q -block, $Q = Q(\vec{\theta})$, as an operator that satisfies:*

1. **Q -fusion:** *For any set of parameters $\vec{\alpha}$ and $\vec{\beta}$, there exist \vec{a} such that*

$$Q(\vec{\alpha}) Q(\vec{\beta}) = Q(\vec{a}), \quad (38)$$

2. **Q -commutation:** *For any set of parameters $\vec{\alpha}$ and $\vec{\beta}$*

$$Q(\vec{\alpha}) B_i(\vec{\beta}) = B_i(\vec{\beta}) Q(\vec{\alpha}), \quad i \neq 2, \quad (39)$$

3. **Q -turnover:** *For any set of parameters $\vec{\alpha}$, $\vec{\beta}$ and $\vec{\gamma}$ there exist \vec{a} , \vec{b} and \vec{c} such that*

$$B_2(\vec{\alpha}) Q(\vec{\beta}) B_2(\vec{\gamma}) = Q(\vec{a}) B_2(\vec{b}) Q(\vec{c}). \quad (40)$$

If the Q - and B_i -blocks satisfy the properties listed above, we will say that $\{Q, B_i\}$ is a Q -block mapping.

The three Q -block properties are illustrated in Fig. 5(a-c). The Q -blocks are not explicitly labeled with an index, as they can only appear in one level, which is at the same height as the first row of B -blocks (see Fig. 5). As can be seen, the Q -block and the block with index 1, i.e. B_1 , satisfy the same properties, and the set of B -block and Q -block rules are symmetric under the exchange $Q \leftrightarrow$

B_1 . This property emerges in the examples we provide in Secs. IV B and IV C, where the Q -block is mapped to a term that corresponds to the controlled version of B_1 .

We are now ready to define a diamond, which is the minimal structure for a quantum circuit that admits a Q -block mapping.

Definition 3 (diamond). Define a “diamond” of height n as,

$$D_n^Q(\vec{\alpha}) := \prod_{m=1}^{(n+1)/2} \left[\prod_{i=n\downarrow}^1 B_i(\vec{\alpha}_{i,2m-1}) \prod_{i=n\downarrow}^2 B_i(\vec{\alpha}_{i,2m}) Q(\vec{\alpha}_{1,2m}) \right],$$

for odd n , and

$$D_n^Q(\vec{\alpha}) := \prod_{m=1}^{n/2} \left[\prod_{i=n\downarrow}^1 B_i(\vec{\alpha}_{i,2m-1}) \prod_{i=n\downarrow}^2 B_i(\vec{\alpha}_{i,2m}) Q(\vec{\alpha}_{1,2m}) \right] \prod_{i=n\downarrow}^1 B_i(\vec{\alpha}_{i,n+1}),$$

for even n . Here \downarrow in the product means that the multiplication is done in the decreasing order, B_i are B -blocks, Q is a Q -block and each term in the product can have different parameters.

An illustration of a diamond of height 5 and 6 are shown in Fig. 5(d) and (e). Next, we prove that a diamond is indeed a minimal realization for a quantum circuit that admits a Q -block mapping by showing that the diamond can absorb any B -block and Q -block.

Theorem 1 (Q -compression). A diamond of height n can be merged with any B -block B_i with $i = 1, 2, \dots, n$ and Q -block Q ,

$$\begin{aligned} D_n^Q(\vec{\alpha}, \vec{\beta}) Q(\vec{\gamma}) &= D_n^Q(\vec{\alpha}, \vec{b}), \\ D_n^Q(\vec{\alpha}, \vec{\beta}) B_i(\vec{\theta}) &= D_n^Q(\vec{u}, \vec{v}). \end{aligned} \quad (41)$$

For odd values of n , merging Q with the diamond requires only one Q -fusion, while merging B_1 requires $n-1$ turnovers and 1 fusion. For even values of n , merging Q with the diamond requires $n-1$ turnovers and 1 fusion, while merging B_1 requires 1 fusion. Merging B_i with $i > 1$ requires $n-i-2$ turnover and 1 merge operations when $n-i$ is even, and $n-i-4$ turnover, 2 Q -turnover and 1 merge operations when $n-i$ is odd.

Proof. The proof is illustrated diagrammatically in Fig. 6. As can be seen, the trajectory that the newly added block follows is similar for both even-odd index and even-odd height cases, with the only difference being the operations that happen on the first row of the diamond.

When the parity of the height and the index i is the same, as demonstrated in Fig. 6(a) and (c), the Q -compression occurs in 3 steps. **Step 1:** a B -block with odd index i is moved all the way to the first row and its index becomes 1 by means of $i-2$ B -block turnover operations. **Step 2:** using the Q -commutation relation $B_1 Q = Q B_1$, it can be passed through Q -block. **Step 3:** then it gets pushed all the way down via $n-1$ turnover operations, and is fused with the corresponding bottom-most block. This adds up to $n-i-2$ turnover operations and 1 fusion operation.

When the height and the index have different parities, as demonstrated in Fig. 6(b) and (d), the Q -compression occurs in 5 steps. **Step 1:** The B -block with index i is first moved to the second row via $i-2$ repeated B -block turnover operations. **Step 2:** Then, it becomes a Q -block via a Q -turnover operation. **Step 3:** it passes through the block with index 1 using Q -commutation rule. **Step 4:** it again becomes a B -block with index 2 using a Q -turnover operation. **Step 5:** it moves all the way down using $n-2$ B -block turnover operations, and is fused with the corresponding bottom-most block. This requires $n-i-4$ B -block turnover operations, 2 Q -turnover operations, and 1 fusion operation. \square

An alternative type of block, which we denote “ P -block”, its block rules and its compression algorithm is presented in Appendix C 1. These rules yield results comparable to those obtained with the Q -block rules. However, they are not as generalizable as Q -block rules.

B. Q -block mapping for Controlled Free Fermions

In this section, we will provide a Q -block mapping that allows us to compress controlled time evolution circuits for any free fermionic model. We will first simplify the controlled time evolution of Eq. (37) without the annihilation and creation terms, i.e. the evolution under the following Hamiltonian,

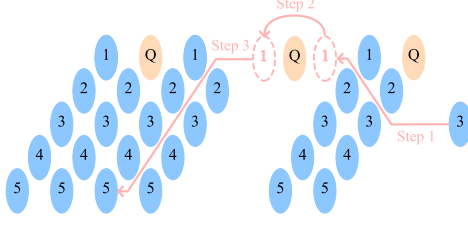
$$\begin{aligned} \mathcal{H}(t) &= \sum_{i,j} (h_{ij}(t) c_i^\dagger c_j + p_{ij}(t) c_i c_j) \\ &+ \mathbf{Z}_0 \sum_{i,j} (\mathbf{h}'_{ij}(\mathbf{t}) \mathbf{c}_i^\dagger \mathbf{c}_j + \mathbf{p}'_{ij}(\mathbf{t}) \mathbf{c}_i \mathbf{c}_j) + \text{H.c.}, \end{aligned} \quad (42)$$

where the new terms are highlighted. We provide the following Q -block mapping for this Hamiltonian:

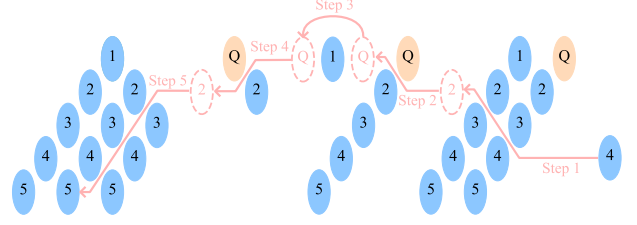
$$\begin{aligned} B_{2i-1}^{\text{TFIM}}(\theta) &= e^{i\theta Z_i}, \\ B_{2i}^{\text{TFIM}}(\theta) &= e^{i\theta X_i X_{i+1}}, \\ Q^{\text{TFIM}}(\theta) &= e^{i\theta Z_0 Z_1}, \end{aligned} \quad (43)$$

which is illustrated in Fig. 7(a). We will show that this mapping indeed covers every interaction term of the Hamiltonian given in Eq. (42), and it satisfies all B -block and Q -block rules.

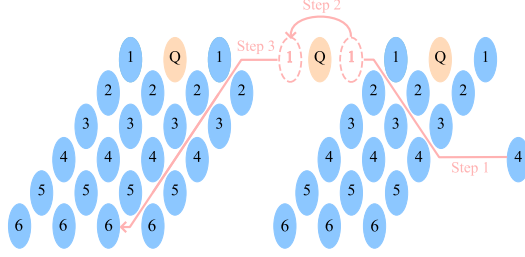
(a) Q-compression (odd height, odd index)



(b) Q-compression (odd height, even index)



(c) Q-compression (even height, even index)



(d) Q-compression (even height, odd index)

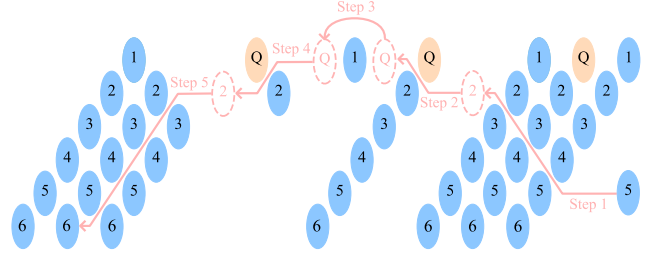
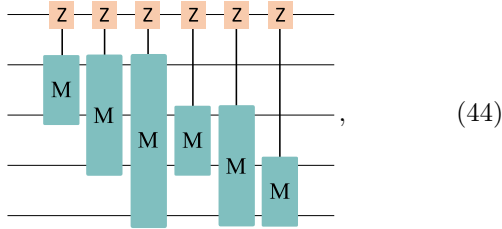


FIG. 6. An illustrative proof of [Thm. 1](#), i.e. how the diamond can absorb a block. Because the Q -diamond structure differs when the height is even or odd, and the operations to absorb a block changes when the index i is even or odd, we illustrate each case in different panels. In panels (a-b), the size of the diamond is $n = 5$, and the index of the block is $i = 3$ on panel (a), and $i = 4$ on panel (b). In panels (c-d), the size of the diamond is $n = 6$, and the index of the block is $i = 4$ on panel (c), and $i = 5$ on panel (d). In panels (a) and (c), the block is absorbed by the Q -diamond structure only via turnover, Q -commutation and fusion operations. On the contrary, the panels (b) and (d) illustrates the cases when a Q -turnover is also required.

Let us show that the set of gates given in [Eq. \(43\)](#) covers all of the new terms given in [Eq. \(42\)](#). When a 1st order Trotter formula is considered, the new terms in bold generate the following structure



with the Z -rotation on the top qubit, which is the ancilla qubit with index 0, coupled to the free fermionic gates from [Eq. \(20\)](#) on every pair of system qubits i, j representing the evolution under the new quadratic terms in [Eq. \(42\)](#). For example,

$$\begin{aligned}
 & \text{Circuit: } \begin{array}{c} \text{--- } Z \text{ ---} \\ | \\ \text{--- } M \text{ ---} \end{array} \equiv e^{i\theta_1 Z_0 Z_1} e^{i\theta_2 Z_0 Z_2} e^{i\theta_3 Z_0 X_1 X_2} \\
 & e^{i\theta_4 Z_0 Y_1 Y_2} e^{i\theta_5 Z_0 Z_1} e^{i\theta_6 Z_0 Z_2},
 \end{aligned} \tag{45}$$

is a Z_0 -controlled free fermionic gate on qubits 1 and 2. Note that the top qubit, i.e. the ancilla qubit, is labeled as the 0th qubit so that the system qubits start at 1, which is consistent with the B -block convention given in [Figs. 1](#) and [3](#).

The gate given in [Eq. \(45\)](#) can be generated via the mapping [Eq. \(43\)](#). The terms that are not directly in the mapping are rotations with the Pauli matrices $Z_0 Z_2$, $Z_0 X_1 X_2$, and $Z_0 Y_1 Y_2$. Using the following relation

$$Z_0 Z_2 = \mathcal{F}_{1,2} Z_0 Z_1 \mathcal{F}_{1,2}^\dagger,$$

we can generate $Z_0 Z_2$ rotation via FSWAP gates which are included in B_i^{TFIM} , and a $Z_0 Z_1$ rotation which is Q^{TFIM} . Similarly, the following relations allow us to generate the rotations with $Z_0 X_1 X_2$ and $Z_0 Y_1 Y_2$ via the mapping [Eq. \(43\)](#):

$$Z_0 X_1 X_2 = e^{i\frac{\pi}{4} Z_1} e^{i\frac{\pi}{4} X_1 X_2} Z_0 Z_1 e^{-i\frac{\pi}{4} X_1 X_2} e^{-i\frac{\pi}{4} Z_1},$$

and

$$Z_0 Y_1 Y_2 = e^{i\frac{\pi}{4} Z_2} e^{i\frac{\pi}{4} X_1 X_2} Z_0 Z_1 e^{-i\frac{\pi}{4} X_1 X_2} e^{-i\frac{\pi}{4} Z_2}.$$

Thus, the controlled fermionic gates on qubits 1 and 2 given in [Eq. \(45\)](#) can be generated via the gates given in [Eq. \(43\)](#).

A generic free fermionic gate on any pair of qubits can be generated via the mapping [Eq. \(43\)](#), by the use of FSWAP gates and [Eq. \(29\)](#). For example, a $Z_0 c_4 c_6$ rotation can be generated via $Z_0 c_1 c_2$ and FSWAP gates

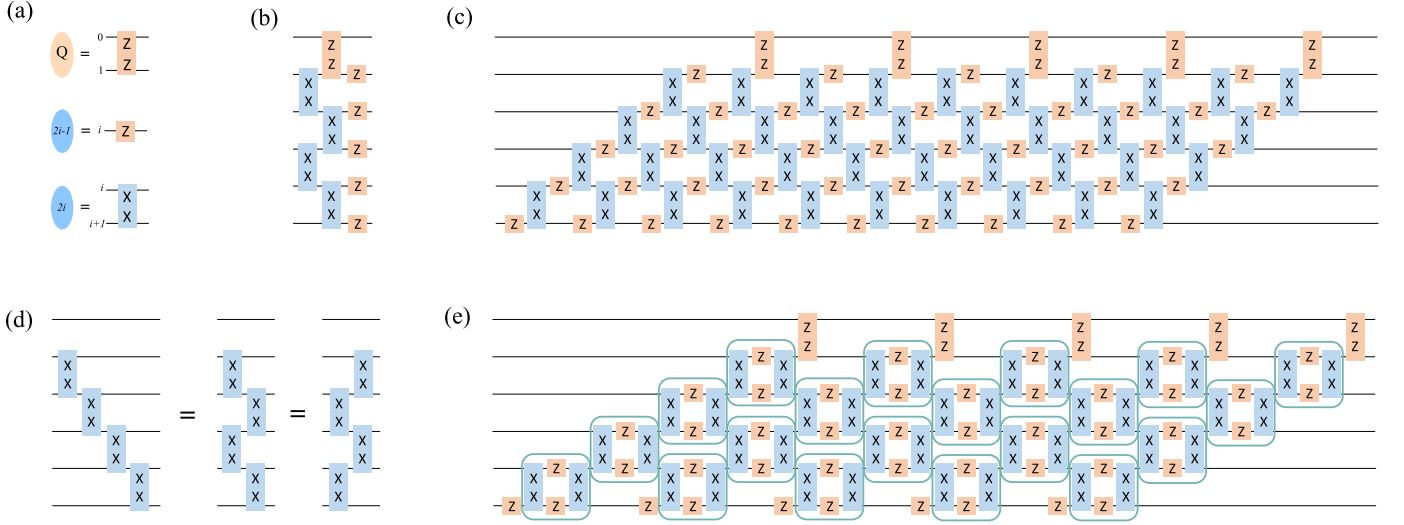


FIG. 7. In panel (a), we show the Q -block mapping that covers the controlled free fermions, where the control qubit is the 0th qubit. Panel (b) shows the complete set of blocks and Q -block for $n = 5$ system qubits and 1 control qubit. In panel (c), we show the final circuit representing the diamond structure (see Def. 3) with this particular Q -block mapping, that can be obtained by using the compression theorems. In this form, the circuit requires $4n(n-1) + 2n = O(4n^2)$ CNOT gates. By using the relation given in panel (d), certain XX gates can be grouped as shown in panel (e). Then, using the relation Eq. (12), these groups can be transformed into free fermionic gates. After this simplification, the number CNOTs is reduced to $2n^2 = O(2n^2)$, which is approximately half of the NOT count of the circuit in panel (c).

in the following way,

$$\begin{array}{c} \text{Z} \\ | \\ \text{M} \\ | \\ \theta \end{array} = \begin{array}{c} \text{Z} \\ | \\ \text{M} \\ | \\ \theta \end{array} \quad (46)$$

Since both FSWAP gates and the $Z_0 c_1 c_2$ gate can be generated via Eq. (43), it follows that every term given in the Hamiltonian Eq. (42) can be generated via the gates given in Eq. (43).

Let us now show that the mapping $\{Q^{\text{TFIM}}, B_i^{\text{TFIM}}\}$ given in Eq. (43) is a Q -block mapping. Because we know that B_i^{TFIM} form a block mapping, we only need to show that Q^{TFIM} satisfy the Q -block mapping rules given in Def. 2 and Fig. 5(a-c). The Q^{TFIM} satisfies the Q -fusion property because of the following

$$Q^{\text{TFIM}}(\alpha)Q^{\text{TFIM}}(\beta) = Q^{\text{TFIM}}(\alpha + \beta). \quad (47)$$

To prove that Q -commutation is satisfied, we need to show that Q^{TFIM} commutes with all B_i^{TFIM} for $i \geq 3$ and $i = 1$. For $i \geq 3$, Q^{TFIM} and B_i^{TFIM} commute simply because they act on different sets of qubits. For $i = 1$, even though they share a qubit, they still commute since $[Z_0 Z_1, Z_1] = 0$. Thus, the mapping satisfies the Q -commutation rule. Finally, to confirm the Q -turnover

relation, we can check the operators in the exponents of Q^{TFIM} and B_2^{TFIM} , i.e., $Z_0 Z_1$ and $X_1 X_2$. These are two anti-commuting Pauli strings, and form the following representation of $\mathfrak{su}(2)$:

$$\mathfrak{su}(2) \equiv \text{ispan}\{Z_0 Z_1, X_1 X_2, Z_0 Y_1 X_2\}. \quad (48)$$

The Euler decomposition of this $\mathfrak{su}(2)$ yields that there exist $a, b, c \in \mathbb{R}$ for any $\alpha, \beta, \gamma \in \mathbb{R}$ such that

$$e^{iaX_1 X_2} e^{ibZ_0 Z_1} e^{icX_1 X_2} = e^{i\alpha Z_0 Z_1} e^{i\beta X_1 X_2} e^{i\gamma Z_0 Z_1}, \quad (49)$$

which is equivalent to

$$\begin{aligned} B_2^{\text{TFIM}}(a)Q^{\text{TFIM}}(b)B_2^{\text{TFIM}}(c) \\ = Q^{\text{TFIM}}(\alpha)B_2^{\text{TFIM}}(\beta)Q^{\text{TFIM}}(\gamma), \end{aligned} \quad (50)$$

where the corresponding angles can be calculated via Eqs. (29) and (30) of [1]. Thus, Q^{TFIM} and B_2^{TFIM} satisfy the Q -turnover property. We conclude that the mapping in Eq. (43) is indeed a Q -block mapping.

This Q -block mapping enables compression of the controlled free fermionic Hamiltonian given in Eq. (42). Using the Q -compression algorithm given in Thm. 1, the fixed depth circuits generated by this mapping for $n = 5$ system qubits and 1 ancilla qubit can be found as Fig. 7(c) and (e). The circuit in Fig. 7(c) is directly obtained from the diamond structure given in Def. 3. It contains n ZZ -rotations and $2n(n-1)$ XX -rotations, which leads to $4n^2 - 2n$ CNOT gates. The number of CNOT gates can be reduced by moving $X_i X_{i+1}$ gates around as shown in Fig. 7(d). This reordering combines certain XX gates, and transforms the circuit from Fig. 7(c) to (e),

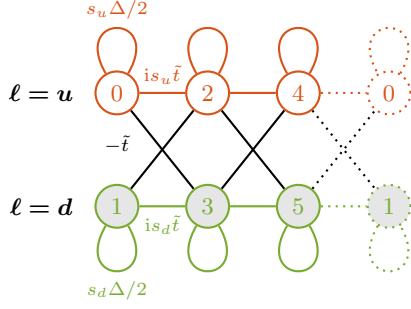


FIG. 8. The 6-site free Creutz-Hubbard model. The terms in the Hamiltonian connecting different sites, i.e. allowing fermions to hop between different sites, are indicated by lines (dashed lines indicate the periodic terms). Self connecting lines correspond to chemical potential terms, parallel lines correspond to the tunnelling terms with phase is_ℓ , and the diagonal black lines correspond to the terms with no phase.

where certain XX gates are grouped together. We can then use Eq. (12), and transform these groups to TFX blocks or free fermionic gates, which can be implemented by only 2 CNOTs instead of 4. Because there are n ZZ gates and $n(n-1)$ groups, the final CNOT count for the circuit in panel (e) becomes $2n + 2n(n-1) = 2n^2$, which is approximately half the CNOT count of the circuit in panel (c).

The same compression can also be achieved with the alternative P -block mapping given in Appendix C 2. This method is capable of generating a CNOT efficient circuit without the usage of TFIM \leftrightarrow TFX transformation, and is more efficient in the case of compression of a few elements due to the $O(n^2)$ overhead of the transformation. However, Q -compression is faster because it is based on TFIM compression, and P -compression if based in TFX compression [2, 23].

We apply our Q -block mapping and Q -compression algorithm to the calculation of a topological phase in the imbalanced Creutz-Hubbard model, which is shown in Fig. 8. The model has two groups of fermions labeled by $\ell \in \{u, d\}$, with on-site energy terms and hopping both within and between the u, d groups. The Hamiltonian of the model is given as the following [61]

$$\mathcal{H} = \sum_{i,\ell} \tilde{t} \left(-c_{i+1,\ell}^\dagger c_{i,\bar{\ell}} + is_\ell c_{i+1,\ell}^\dagger c_{i,\ell} + \text{H.c.} \right) + \sum_{i,\ell} \frac{\Delta}{2} s_\ell c_{i,\ell}^\dagger c_{i,\ell}, \quad (51)$$

where $\ell \in \{u, d\}$ and $\bar{\ell}$ is the opposite choice, i.e. if $\ell = u$, then $\bar{\ell} = d$ and vice versa. We set $s_u = 1$ and $s_d = -1$. The term proportional to Δ creates an imbalance between two parts of the ladder.

The model has a topological phase transition at the value of $\Delta = 4\tilde{t}$, and the order parameter of this transition is called the “Zak phase” [61]. The Zak phase is

defined as the following

$$\phi_{\text{Zak}} := \int_{\text{BZ}} dq \langle q | \partial_q | q \rangle, \quad (52)$$

where $|q\rangle$ is the single particle state with quasi-momentum value q , and the integral is taken over the Brillouin zone $[-\pi, \pi]$. For the Hamiltonian given in Eq. (51), the Zak phase can be analytically calculated to be

$$\phi_{\text{Zak}} = \pi\theta(4\tilde{t} - \Delta). \quad (53)$$

For $\Delta < 4\tilde{t}$, the Zak phase is non-zero, and the model shows a topologically non-trivial behavior [61].

Numerical calculations of the Zak phase require a discretized integral over the Brillouin zone, which is problematic when only a few sites are used; the available momenta for an N -site periodic lattice are $k_n = 2\pi n/N$ with $n = 0, 1, \dots, N-1$. This problem can be circumvented by employing twisted boundary conditions [62, 63]. By modifying the boundary hopping terms with an angle $\exp i\varphi$ the allowed momentum values become $k_n(\varphi) = 2\pi n/N + \varphi/N$. Thus, if we vary the twist angle from 0 to 2π , we run through all momentum values, without requiring a larger unit cell, and while remaining in real space. Measuring the Zak phase then can be done by multiplying the overlap amongst the ground states of the Creutz-Hubbard Hamiltonian with different twist angles. To obtain the ground states, we use adiabatic evolution which starts from the ground state of a Creutz-Hubbard model with $\Delta \gg \tilde{t}$. In this case, the imbalance term dominates, and the ground state becomes very close to the state $|\psi_0\rangle = |0101\dots 0101\rangle$, where the d sites are occupied and u sites are empty. The Δ value is then adiabatically evolved to the desired value, to obtain the ground state of $\mathcal{H}(\varphi = 0)$ with twist angle $\varphi = 0$. Then the twist angle is adiabatically evolved to $\varphi = 2\pi$. By doing so, we produce the ground state for a given set of twist angle values $\{\varphi_i\}$, and the desired imbalance Δ value. The Zak phase can then be approximated by the following:

$$e^{i\phi_{\text{Zak}}} = \prod_i \langle \varphi_i | \varphi_{i+1} \rangle, \quad (54)$$

where $|\varphi_i\rangle$ is the ground state of the Creutz-Hubbard Hamiltonian $\mathcal{H}(\varphi_i)$ with twist angle φ_i . This approximation becomes exact when φ_i form a uniform continuous set.

Let us define a unitary U_i such that $|\varphi_i\rangle = U_i |\psi_0\rangle$ where $|\psi_0\rangle = |0101\dots 0101\rangle$ is the ground state of the imbalance term. Since we generate the state via adiabatic time evolution, this U_i consists of free fermionic evolution. By using the TFX block mapping given in Fig. 1(g) and the compression given in Fig. 1(d), this free fermionic evolution can be compressed down to a TFX triangle. The transition amplitude given in Eq. (54) reads $\langle \varphi_i | \varphi_{i+1} \rangle = \langle \psi_0 | U_i^\dagger U_{i+1} | \psi_0 \rangle$. Since both U_i and U_{i+1} can

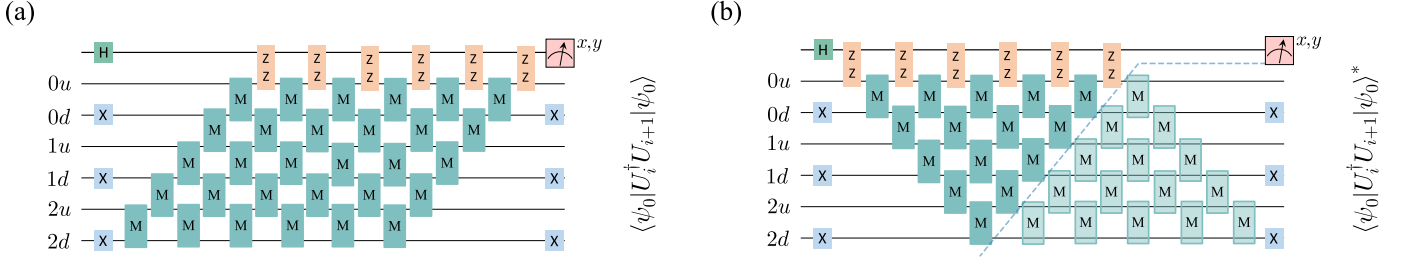


FIG. 9. (a) The Hadamard test circuit to calculate the free fermionic overlap. The controlled free fermionic evolution is compressed down to a diamond structure as given in Fig. 7(e), where we did replace the groups with the free fermionic gates. (b) By just taking the complex conjugation of the overlap, the circuit can be inverted. Because the Hadamard test requires only the measurement of the ancilla qubit, approximately half of the circuit (the free fermionic gates below the diagonal dashed line) can be neglected.

be represented as a TFXY triangle, $U_i^\dagger U_{i+1}$ also can be compressed into a TFXY triangle. This transition amplitude can be calculated via the Hadamard test. In order to do so, one needs to implement a circuit in which the back and forth evolution $U_i^\dagger U_{i+1}$ is implemented if and only if the ancilla qubit is in state $|1\rangle$, which requires controlled free fermionic evolution, and can be compressed into a diamond circuit as shown in Fig. 7.

After obtaining the diamond for the overlap $\langle \psi_0 | U_i^\dagger U_{i+1} | \psi_0 \rangle$, shown in Fig. 9(a), we can invert the circuit to instead compute the overlap $\langle \psi_0 | U_i^\dagger U_{i+1} | \psi_0 \rangle^*$ (Fig. 9(b)) from which we can obtain the Zak phase via complex conjugation. As we are only measuring the ancilla qubit in a Hadamard test, we can discard the gates that have no effect on the measurement result of the inverted circuit, thereby reducing the number of CNOT gates by half. Note that for computing the overlap in any free fermionic calculation, the Hadamard test circuit

will have the same diamond form, and can be simplified via this complex conjugation method.

Our detailed protocol is as follows. We first initialize our system with a large value of $\Delta_0 = 200\tilde{t}$. In this case, the imbalance term dominates, and the ground state is the half-filled state where all the particles live in the down lattice sites labelled d . We adiabatically change Δ_0 to the target value Δ for our Zak phase calculation, giving us the ground state for $\varphi = 0$. Then, we change the φ angle from 0 to 2π . Classical simulations show that it is sufficient to use 5 values for φ , i.e. using $d\varphi = 2\pi/5$. For all the evolution, the controlled compression is used, and thus we have a diamond structure (c.f. Fig. 7). We use these diamond structures to calculate the overlap between adjacent ground states as in the right hand side of Eq. (54), which when multiplied yields the Zak phase for the Δ .

We first used Quantinuum's H1-1E emulator which closely mimics the H1 QPU hardware, to simulate the Zak phase of the 6-site Creutz-Hubbard model using 7 qubits and 1,000 shots to obtain the necessary statistics. The results were found to be in good agreement with the analytical results. We subsequently used Quantinuum's H1-1 quantum hardware to compute the Zak phase for the different Δ values [64]. Here we used only 200 shots to extract the Zak phase. Both the simulator and hardware results are shown together with noise free simulation results in Fig. 10. We observe that the imaginary part of the phase exhibits a jump from $-\pi$ to 0 across $\Delta = 4\tilde{t}$, illustrating that the topological phase transition is properly captured in these calculations. The results from the hardware are in close agreement with the emulator results and noise free results, providing confidence that the Zak phase can be accurately obtained with trapped ion quantum computers. The real part of the phase encodes the decay in the wavefunction overlap in Eq. (54). In the limit $d\varphi \rightarrow 0$ and with perfect hardware, the real part should be identically zero. Here, due to finite $d\varphi$ and hardware noise, some decay is present, but this does not affect the calculation of the geometric Zak phase, i.e. $\text{Im } i\phi_{\text{Zak}}$.

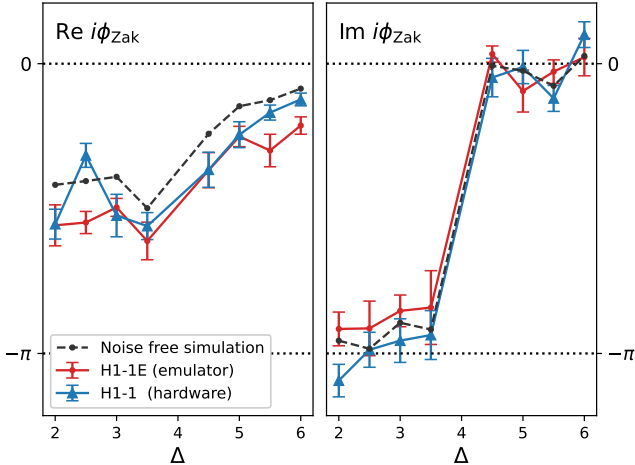


FIG. 10. Real and imaginary parts of $i\phi_{\text{Zak}}$ obtained via Eq. (54), using 5 total states. The imaginary part shows a topological phase transition, switching from $-\pi$ to 0 at $\Delta = 4$. The real part is non-zero due to the finite twist angle step $d\varphi = 2\pi/5$ (see text for more details).

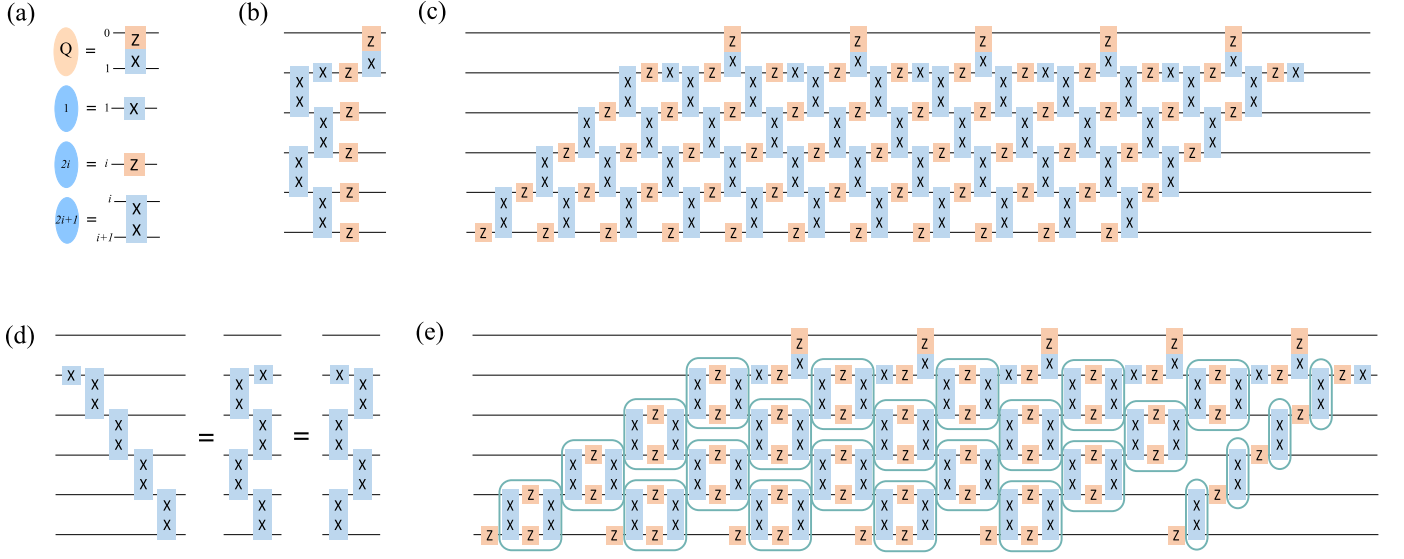


FIG. 11. In panel (a), we show the Q -block mapping that covers the controlled free fermions with creation, where the control qubit is the 0th qubit. Panel (b) shows the complete set of blocks and Q -block for $n = 5$ system qubits and 1 control qubit. In panel (c), we show the final circuit representing the diamond structure (see Def. 3) with this particular Q -block mapping, that can be obtained by using the compression theorems. In this form, the circuit requires $4n(n-1) + 4n - 2 = O(4n^2)$ CNOT gates. By using the relation given in panel (d), certain XX and X gates can be grouped as shown in panel (e). Then, using the relation Eq. (12), these groups can be transformed into free fermionic gates. After this simplification, the number CNOTs is reduced to $2n^2 + 2n - 2 = O(2n^2)$, which is approximately half of the NOT count of the circuit in panel (c).

C. Q -block mapping for Controlled Free Fermions with Creation

In this section, we will provide a Q -block mapping that allows us to compress controlled time evolution circuits for any free fermionic model, including the ones with creation and annihilation operators as discussed previously in Sec. III B for the uncontrolled case. In this setting, the system can be described by the following Hamiltonian

$$\begin{aligned} \mathcal{H}(t) = & \sum_{i,j} (h_{ij}(t) c_i^\dagger c_j + p_{ij}(t) c_i c_j) + \sum_i \mathbf{q}_i(t) \mathbf{c}_i \\ & + Z_0 \sum_{i,j} (h'_{ij}(t) c_i^\dagger c_j + p'_{ij}(t) c_i c_j) \\ & + \mathbf{Z}_0 \sum_i \mathbf{q}'_i(t) \mathbf{c}_i + \text{H.c.}, \end{aligned} \quad (55)$$

where the last H.c. implies the hermitian conjugate of the entire right-hand side. The new terms compared to the Hamiltonian given in Eq. (42) are creation/annihilation and controlled creation/annihilation terms, and are denoted with bold font. We provide the following Q -block mapping to compress the evolution under this Hamiltonian into a diamond:

$$\begin{aligned} B_1^{\text{CTFIM}}(\theta) &= e^{i\theta X_1}, \\ B_{2i}^{\text{CTFIM}}(\theta) &= e^{i\theta Z_i}, \\ B_{2i+1}^{\text{CTFIM}}(\theta) &= e^{i\theta X_i X_{i+1}}, \\ Q^{\text{CTFIM}}(\theta) &= e^{i\theta Z_0 X_1}, \end{aligned} \quad (56)$$

where the superscript CTFIM stands for creation TFIM, implying that this mapping contains the fermionic creation and annihilation terms, and the free fermion terms are implemented via TFIM gates. An illustration of this mapping is given in Fig. 11(a).

Let us show that every term in the Hamiltonian given in Eq. (55) can be implemented via the gates given in Eq. (56). As we know from Sec. III B, the blocks B_i^{CTFIM} cover all the uncontrolled terms, i.e. the terms that do not have a Z_0 attached. The following relation of the exponent of Q^{CTFIM} show that the mapping Eq. (56) can implement creation/annihilation of a fermion on site 1 in a controlled fashion:

$$\begin{aligned} B_2^{\text{CTFIM}}(\theta) Z_0 X_1 B_2^{\text{CTFIM}}(-\theta) &= \cos 2\theta Z_0 X_1 + \sin 2\theta Z_0 Y_1 \\ &= Z_0 \left(e^{2i\theta} c_1 + e^{-2i\theta} c_1^\dagger \right). \end{aligned} \quad (57)$$

With the usage of FSWAP gates, we can then cover all controlled creation/annihilation terms with the mapping in Eq. (56). The following relation shows that Q^{TFIM} from the TFIM Q -block mapping in Eq. (43) can be generated via our new CTFIM mapping:

$$Z_0 X_1 = e^{i\frac{\pi}{4} X_1} e^{i\frac{\pi}{4} Z_1} Z_0 X_1 e^{-i\frac{\pi}{4} Z_1} e^{-i\frac{\pi}{4} X_1}, \quad (58)$$

which yields

$$\begin{aligned} Q^{\text{TFIM}}(\theta) &= B_1^{\text{CTFIM}}(\pi/4) B_2^{\text{CTFIM}}(\pi/4) Q^{\text{CTFIM}}(\theta) \\ &B_2^{\text{CTFIM}}(-\pi/4) B_1^{\text{CTFIM}}(-\pi/4). \end{aligned} \quad (59)$$

Since B_i^{CTFIM} contains all B_i^{TFIM} as well, the mapping Eq. (56) then contains the Q -block mapping given in Eq. (43), and thus can implement all controlled fermion pair operations $Z_0 c_i^{(\dagger)} c_j^{(\dagger)}$ in the Hamiltonian Eq. (55) as well.

Let us show that the CTFIM mapping is a Q -block mapping. From Sec. IIIB, we know that the CTFIM blocks B_i^{CTFIM} satisfy the block properties and form a B -block mapping. We only need to show that Q^{CTFIM} satisfy the Q -block properties given in Fig. 5(a-c). The Q -fusion property is satisfied due to the following:

$$Q^{\text{CTFIM}}(\alpha)Q^{\text{CTFIM}}(\beta) = Q^{\text{CTFIM}}(\alpha + \beta). \quad (60)$$

To prove that Q -commutation is satisfied, we need to show that Q^{CTFIM} commutes with all B_i^{CTFIM} for $i \geq 3$ and $i = 1$. For $i \geq 4$, Q^{CTFIM} and B_i^{CTFIM} commute simply because they act on different sets of qubits. For $i = 1$ and 3, even though they share a qubit, they still commute since $[Z_0 X_1, X_1] = 0$ and $[Z_0 X_1, X_1 X_2] = 0$ respectively. Thus, the mapping satisfy the Q -commutation rule. Finally, the exponents of Q^{CTFIM} and B_2^{CTFIM} , which are $Z_0 X_1$ and Z_1 , form the following representation of $\mathfrak{su}(2)$:

$$\mathfrak{su}(2) \equiv \text{ispan}\{Z_0 X_1, Z_1, Z_0 Y_1\}. \quad (61)$$

The Euler decomposition of this $\mathfrak{su}(2)$ yields that there exist $a, b, c \in \mathbb{R}$ for any $\alpha, \beta, \gamma \in \mathbb{R}$ such that

$$e^{iaX_1 X_2} e^{ibZ_0 Z_1} e^{icX_1 X_2} = e^{i\alpha Z_0 Z_1} e^{i\beta X_1 X_2} e^{i\gamma Z_0 Z_1}, \quad (62)$$

which is equivalent to

$$\begin{aligned} B_2^{\text{TFIM}}(a)Q^{\text{TFIM}}(b)B_2^{\text{TFIM}}(c) \\ = Q^{\text{TFIM}}(\alpha)B_2^{\text{TFIM}}(\beta)Q^{\text{TFIM}}(\gamma), \end{aligned} \quad (63)$$

where the corresponding angles can be calculated via Eqs. (29) and (30) of [1]. Thus, Q^{CTFIM} and B_1^{CTFIM} satisfy the Q -turnover property as well. We conclude that the mapping given in Eq. (56) is indeed a Q -block mapping, and by Thm. 1, time evolution under the Hamiltonian in Eq. (55) can be compressed into a diamond.

Fig. 11 illustrates the Q -block mapping and the fixed depth circuits obtained by the Q -compression theorem Thm. 1. Fig. 11(a) illustrates Eq. (56) diagrammatically, where on the left hand side we have the blocks, and on the right hand side we have the gates. Fig. 11(b) illustrates all blocks and Q -block on $n = 5$ system and 1 ancilla qubits for the Hamiltonian in Eq. (55). As it can be seen, there is 1 Q -block and $2n = 10$ blocks present for this model and Q -block mapping. In panel (c), we show the final circuit representing the diamond structure (see Def. 3) with this particular Q -block mapping, that can be obtained by using the compression theorems. In this form, the circuit requires $4n(n - 1) + 4n - 2 = O(4n^2)$ CNOT gates. By using the relation given in panel (d), certain XX and X gates can be grouped as shown in panel (e). Then, using the relation Eq. (12), these groups can be transformed into free fermionic gates. After this

simplification, the number CNOTs is reduced to $2n^2 + 2n - 2 = O(2n^2)$, which is approximately half of the CNOT count of the circuit in panel (c).

This mapping illustrates another advantage of Q -blocks over P -blocks given in Appendix C, because P -blocks cannot be generalized to compress the time evolution under the Hamiltonian given in Eq. (55).

V. DISCUSSION AND OUTLOOK

With the developments in this paper, we have significantly extended the class of Hamiltonians whose evolution may be compressed. Specifically, any time dependent mean field Hamiltonian on an arbitrary lattice can now be simulated efficiently, such as the tight binding model with any particle number, superconducting free fermions, free fermions with particle injection, controlled free fermions on any lattice, and as given in Appendix B, certain spin models such as TFIM and TFX on a ring. In addition to that, we can add and remove particles on a given mode with any amplitude. In Ref. [10] it was shown that for momentum conserving Hamiltonians, obtaining Green's functions directly in the momentum basis via perturbing the system with c_k^\dagger yields less noisy results compared to obtaining perturbing with c_r^\dagger and post-processing via Fourier transformation. Accordingly, we provide a direct method for creating one or more particles with definite momenta in Appendix A. For other systems, such as those that arise in chemistry, these single particle modes are more general. Our methods can easily be generalized to these modes as well, and be used to compress particle creation/annihilation operators on any mode. With the addition of controlled evolution, these techniques are now applicable in a broader regime. Controlled evolution is a key step in quantum phase estimation, and similarly plays a role in computing Hamiltonian matrix elements for real time subspace expansions [65–67].

The compression algorithm discussed here is not limited to compressing time evolution. Rather, it may be applied to any set of quantum gates that obey the B -block and Q -block properties. As long as the block mapping can be found, the algorithms developed here can be readily applied. We do not expect that general state preparation or other similar algorithms can be fully compressed, as the compressed circuits lack expressibility; the states that can be reached are limited [23, 68]. However, there may be sizable subsets of the full quantum circuits whose elements do obey the block properties, and may be significantly shortened. We expect that the developments made in this work can thus have significant impact in transpiler software.

The compression software is available as part of the fast free fermion compiler (F3C) [40, 41] at <https://github.com/QuantumComputingLab>. F3C is based on the QCLAB toolbox [42, 43] for creating and representing quantum circuits.

ACKNOWLEDGMENTS

EK and AFK were supported by the National Science Foundation under award No. 1818914: PFCQC: STAQ: Software-Tailored Architecture for Quantum co-design and No. 2325080: PIF: Software-Tailored Architecture for Quantum Co-Design. LBO, RVB, and WAdJ were supported by the U.S. Department of Energy (DOE) under Contract No. DE-AC02-05CH11231, through the Office of Advanced Scientific Computing Research Accelerated Research for Quantum Computing Program. This research used resources of the National Energy Research

Scientific Computing Center (NERSC), a U.S. Department of Energy Office of Science User Facility located at Lawrence Berkeley National Laboratory, operated under Contract No. DE-AC02-05CH11231. This research used resources of the Oak Ridge Leadership Computing Facility, which is a DOE Office of Science User Facility supported under Contract No. DE-AC05-00OR22725. We acknowledge the use of IBM Quantum services for this work. Finally, we acknowledge the use of the QISKIT software package for use in the quantum computer calculations [69].

-
- [1] E. Kökcü, D. Camps, L. Bassman Oftelie, J. K. Freericks, W. A. de Jong, R. Van Beeumen, and A. F. Kemper, *Physical Review A* **105**, 032420 (2022).
 - [2] D. Camps, E. Kökcü, L. Bassman Oftelie, W. A. De Jong, A. F. Kemper, and R. Van Beeumen, *SIAM Journal on Matrix Analysis and Applications* **43**, 1084 (2022).
 - [3] A. Chiesa, F. Tacchino, M. Grossi, P. Santini, I. Tavernelli, D. Gerace, and S. Carretta, *Nature Physics* **15**, 455 (2019).
 - [4] A. Roggero and J. Carlson, *Phys. Rev. C* **100**, 034610 (2019).
 - [5] A. Francis, J. K. Freericks, and A. F. Kemper, *Phys. Rev. B* **101**, 014411 (2020).
 - [6] T. Kosugi and Y. I. Matsushita, *Physical Review A* **101**, 1 (2020).
 - [7] T. Kosugi and Y.-i. Matsushita, *Phys. Rev. Research* **2**, 033043 (2020).
 - [8] S. Endo, I. Kurata, and Y. O. Nakagawa, *Phys. Rev. Research* **2**, 033281 (2020).
 - [9] F. Libbi, J. Rizzo, F. Tacchino, N. Marzari, and I. Tavernelli, arXiv preprint arXiv:2203.12372 (2022).
 - [10] E. Kökcü, H. A. Labib, J. Freericks, and A. F. Kemper, arXiv preprint arXiv:2302.10219 (2023).
 - [11] T. Steckmann, T. Keen, E. Kökcü, A. F. Kemper, E. F. Dumitrescu, and Y. Wang, *Physical Review Research* **5**, 023198 (2023).
 - [12] K. Joven and V. Bastidas, arXiv preprint arXiv:2405.12289 (2024).
 - [13] M. Rodriguez-Vega, E. Carlander, A. Bahri, Z.-X. Lin, N. A. Sinitsyn, and G. A. Fiete, *Physical Review Research* **4**, 013196 (2022).
 - [14] X. Zhang, W. Jiang, J. Deng, K. Wang, J. Chen, P. Zhang, W. Ren, H. Dong, S. Xu, Y. Gao, *et al.*, *Nature* **607**, 468 (2022).
 - [15] X. Mi, M. Ippoliti, C. Quintana, A. Greene, Z. Chen, J. Gross, F. Arute, K. Arya, J. Atalaya, R. Babbush, *et al.*, *Nature* **601**, 531 (2022).
 - [16] V. V. Shende, S. S. Bullock, and I. L. Markov, *IEEE Transactions on Computer-Aided Design of Integrated Circuits and Systems* **25**, 1000 (2006).
 - [17] N. Khaneja and S. J. Glaser, *Chemical Physics* **267**, 11 (2001).
 - [18] B. Drury and P. Love, *Journal of Physics A: Mathematical and Theoretical* **41**, 395305 (2008).
 - [19] B. Commeau, M. Cerezo, Z. Holmes, L. Cincio, P. J. Coles, and A. Sornborger, arXiv preprint arXiv:2009.02559 (2020).
 - [20] L. Bassman Oftelie, R. Van Beeumen, E. Younis, E. Smith, C. Iancu, and W. A. de Jong, *Materials Theory* **6**, 13 (2022).
 - [21] Y. Zhang, R. Wiersema, J. Carrasquilla, L. Cincio, and Y. B. Kim, arXiv preprint arXiv:2409.16346 (2024).
 - [22] H. N. Sá Earp and J. K. Pachos, *Journal of mathematical physics* **46**, 082108 (2005).
 - [23] E. Kökcü, T. Steckmann, Y. Wang, J. Freericks, E. F. Dumitrescu, and A. F. Kemper, *Physical Review Letters* **129**, 070501 (2022).
 - [24] D. Wierichs, M. West, R. T. Forestano, M. Cerezo, and N. Killoran, arXiv preprint arXiv:2503.19014 (2025).
 - [25] D. W. Berry, G. Ahokas, R. Cleve, and B. C. Sanders, *Comm. Math. Phys.* **270**, 359 (2007).
 - [26] Y. Atia and D. Aharonov, *Nature communications* **8**, 1 (2017).
 - [27] S. Gu, R. D. Somma, and B. Şahinoğlu, *Quantum* **5**, 577 (2021).
 - [28] I. D. Kivlichan, J. McClean, N. Wiebe, C. Gidney, A. Aspuru-Guzik, G. K.-L. Chan, and R. Babbush, *Phys. Rev. Lett.* **120**, 110501 (2018).
 - [29] Z. Jiang, K. J. Sung, K. Kechedzhi, V. N. Smelyanskiy, and S. Boixo, *Phys. Rev. Applied* **9**, 044036 (2018).
 - [30] F. Arute, K. Arya, R. Babbush, D. Bacon, J. C. Bardin, R. Barends, S. Boixo, M. Broughton, B. B. Buckley, D. A. Buell, *et al.*, *Science* **369**, 1084 (2020).
 - [31] B. Peng, S. Gulania, Y. Alexeev, and N. Govind, *Physical Review A* **106**, 012412 (2022).
 - [32] S. Gulania, Z. He, B. Peng, N. Govind, and Y. Alexeev, in *2022 IEEE/ACM 7th Symposium on Edge Computing (SEC)* (2022) pp. 406–410.
 - [33] L. B. Oftelie, R. Van Beeumen, D. Camps, W. A. de Jong, and M. Dupont, arXiv preprint arXiv:2210.08386 (2022).
 - [34] M. Dupont, N. Didier, M. J. Hodson, J. E. Moore, and M. J. Reagor, *Physical Review A* **106**, 022423 (2022).
 - [35] A. Sopena, M. H. Gordon, D. García-Martín, G. Sierra, and E. López, *Quantum* **6**, 796 (2022).
 - [36] G. Jian, Y. Yang, Z. Liu, Z.-G. Zhu, and Z. Wang, *Europhysics Letters* **141**, 10003 (2023).
 - [37] G. Hao Low, Y. Su, Y. Tong, and M. C. Tran, *arXiv e-prints*, arXiv:2211.09133 (2022), arXiv:2211.09133 [quant-ph].
 - [38] T. N. Kaldenbach, M. Heller, G. Alber, and V. M. Stojanovic, *arXiv e-prints*, arXiv:2211.02684 (2022), arXiv:2211.02684 [quant-ph].

- [39] A. Barenco, C. H. Bennett, R. Cleve, D. P. DiVincenzo, N. Margolus, P. Shor, T. Sleator, J. A. Smolin, and H. Weinfurter, *Phys. Rev. A* **52**, 3457 (1995).
- [40] D. Camps and R. Van Beeumen, *F3C* (2021), version 0.1.0.
- [41] R. Van Beeumen and D. Camps, *F3C++* (2021), version 0.1.0.
- [42] D. Camps and R. Van Beeumen, *QCLAB* (2021), version 0.1.2.
- [43] R. Van Beeumen and D. Camps, *QCLAB++* (2021), version 0.1.2.
- [44] M. A. Nielsen and I. L. Chuang, *Quantum computation and quantum information* (Cambridge university press, 2010).
- [45] I. Magoulas and F. A. Evangelista, *Journal of Chemical Theory and Computation* **19**, 822 (2023).
- [46] A. M. Projansky, J. Necaie, and J. D. Whitfield, arXiv preprint arXiv:2410.10068 (2024).
- [47] R. Jozsa and A. Miyake, *Proceedings of the Royal Society A: Mathematical, Physical and Engineering Sciences* **464**, 3089 (2008).
- [48] G. Vidal and C. M. Dawson, *Physical Review A* **69**, 010301 (2004).
- [49] A. H. Karamlou, J. Braumüller, Y. Yanay, A. Di Paolo, P. M. Harrington, B. Kannan, D. Kim, M. Kjaergaard, A. Melville, S. Muschinske, *et al.*, *npj Quantum Information* **8**, 35 (2022).
- [50] P. W. Anderson, *Phys. Rev.* **109**, 1492 (1958).
- [51] V. Bucaj, arXiv:1608.01379 (2016).
- [52] P. D. Nation, H. Kang, N. Sundaresan, and J. M. Gambetta, *PRX Quantum* **2**, 040326 (2021).
- [53] L. Viola and S. Lloyd, *Physical Review A* **58**, 2733 (1998).
- [54] P. Zanardi, *Physics Letters A* **258**, 77 (1999).
- [55] D. Vitali and P. Tombesi, *Physical Review A* **59**, 4178 (1999).
- [56] L.-M. Duan and G.-C. Guo, *Physics Letters A* **261**, 139 (1999).
- [57] B. Pokharel, N. Anand, B. Fortman, and D. A. Lidar, *Physical review letters* **121**, 220502 (2018).
- [58] J. Surace and L. Tagliacozzo, *SciPost Physics Lecture Notes*, 054 (2022).
- [59] M. Collura, J. De Nardis, V. Alba, and G. Lami, arXiv preprint arXiv:2412.05367 (2024).
- [60] A. Francis, E. Zelleke, Z. Zhang, A. F. Kemper, and J. K. Freericks, *Symmetry* **14**, 809 (2022).
- [61] J. Jünemann, A. Piga, S.-J. Ran, M. Lewenstein, M. Rizzi, and A. Bermúdez, *Physical Review X* **7**, 031057 (2017).
- [62] Q. Niu, D. J. Thouless, and Y.-S. Wu, *Physical Review B* **31**, 3372 (1985).
- [63] X. Xiao, J. Freericks, and A. Kemper, *Quantum* **7**, 987 (2023).
- [64] Quantinuum H1-1. <https://www.quantinuum.com/>, October 26-31, 2023.
- [65] K. Klymko, C. Mejuto-Zaera, S. J. Cotton, F. Wudarski, M. Urbanek, D. Hait, M. Head-Gordon, K. B. Whaley, J. Moussa, N. Wiebe, *et al.*, *PRX Quantum* **3**, 020323 (2022).
- [66] Y. Shen, D. Camps, A. Szasz, S. Darbha, K. Klymko, D. B. Williams-Young, N. M. Tubman, and R. Van Beeumen, in *2023 IEEE International Conference on Quantum Computing and Engineering (QCE)*, Vol. 2 (IEEE, 2023) pp. 302–303.
- [67] Y. Shen, A. Buzali, H.-Y. Hu, K. Klymko, D. Camps, S. F. Yelin, and R. Van Beeumen, arXiv preprint arXiv:2409.13691 (2024).
- [68] D. d'Alessandro, *Introduction to quantum control and dynamics* (CRC press, 2007).
- [69] M. Treinish, J. Gambetta, S. Thomas, P. Nation, qiskit bot, P. Kassebaum, D. M. Rodríguez, S. de la Puente González, J. Lishman, S. Hu, L. Bello, K. Krulich, J. Garrison, J. Yu, M. Marques, J. Gacon, D. McKay, J. Gomez, L. Capelluto, Travis-S-IBM, A. Mitchell, A. Panigrahi, lerongil, R. I. Rahman, S. Wood, T. Itoko, A. Pozas-Kerstjens, C. J. Wood, D. Singh, and D. Risinger, *Qiskit/qiskit: Qiskit 0.41.0* (2023).

Appendix A: Fermion Creation with Definite Momentum

One of the interesting features we can exploit from the compressibility of the evolution under Eq. (18) is that it allows us to create/annihilate particles in any single particle mode in a unitary fashion. Here, we will specifically show how to generate a circuit that creates a particle with a definite momentum k .

Creation operators in momentum space c_k^\dagger are a discrete Fourier transformation of creation operators in position space c_r^\dagger :

$$c_k^\dagger = \sum_{r=1}^n e^{2\pi i k r / n} c_r^\dagger, \quad (\text{A1})$$

where $k = 0, 1, 2, \dots, n-1$ and n is the number of lattice sites. The c_k satisfy the anti-commutation relations $\{c_p, c_k\} = \{c_p^\dagger, c_k^\dagger\} = 0$ and $\{c_p, c_k^\dagger\} = \delta_{pq}$ where δ_{pq} is the Kronecker delta.

The state we would like to create is $|\psi_k\rangle = c_k^\dagger |0\rangle$ where $|0\rangle$ represents the empty fermion state, which is $|000\dots 0\rangle$ in the computational basis. Unfortunately c_k^\dagger is not a unitary operator. However, $c_k^\dagger + c_k$ is Hermitian and due to the anti-commutation relations, we have $(c_k^\dagger + c_k)^2 = 1$. Moreover, $c_k |0\rangle = 0$. Combining these, we have

$$e^{i\theta(c_k^\dagger + c_k)} |0\rangle = \cos(\theta) |0\rangle + i \sin(\theta) (c_k^\dagger + c_k) |0\rangle = \cos(\theta) |0\rangle + i \sin(\theta) |\psi_k\rangle. \quad (\text{A2})$$

For $\theta = \pi/2$, we obtain ψ_k up to a global phase

$$e^{i\frac{\pi}{2}(c_k^\dagger + c_k)} |0\rangle = i |\psi_k\rangle. \quad (\text{A3})$$

Thus, if we implement time evolution unitary under $\mathcal{H}_k = c_k^\dagger + c_k$ for time $t = -\pi/2$, we can create a particle with momentum k . Now, this Hamiltonian is a special case for the Hamiltonian in Eq. (18), and therefore we can generate a circuit via Trotter decomposition and compress it into a fixed depth circuit.

This method is not limited to creating a single particle. One can use the same unitary with different momentum p to add another particle. Because $|\psi_k\rangle$ does not contain any particle with momentum $p \neq k$, $c_p |\psi_k\rangle = 0$ still holds, and we can obtain

$$e^{i\frac{\pi}{2}(c_p^\dagger + c_p)} e^{i\frac{\pi}{2}(c_k^\dagger + c_k)} |0\rangle = i e^{i\frac{\pi}{2}(c_p^\dagger + c_p)} |\psi_k\rangle = -(c_p^\dagger + c_p) |\psi_k\rangle = -c_p^\dagger |\psi_k\rangle = -c_p^\dagger c_k^\dagger |0\rangle. \quad (\text{A4})$$

This corresponds to first evolving under $\mathcal{H}_k = c_k^\dagger + c_k$, then under $\mathcal{H}_p = c_p^\dagger + c_p$. This is still a special case of one evolution under the time dependent Hamiltonian Eq. (18). Switching from \mathcal{H}_k to \mathcal{H}_p is just changing coefficients via simulation time. This can be applied for different creating more particles with different momenta as well. Thus we can create any number of particles with different momenta via using the compression of Eq. (18).

As a remark, this is not limited to creating momentum definite states. This can be done for any orthonormal single particle basis simply by changing the coefficients of Eq. (A1).

Appendix B: Q -block Mappings for 1-D Spin Models with Periodic Boundary Condition

1. TFIM with Periodic Boundary Condition

Consider the following TFIM Hamiltonian with periodic boundary condition

$$\mathcal{H}(t) = \sum_{i=1}^n \tilde{J}_i(t) X_i X_{i+1} + \sum_{i=1}^n \tilde{h}_i(t) Z_i \quad (\text{B1})$$

where $X_{n+1} := X_1$. We know that if it was not periodic but open boundary condition, the evolution under the Hamiltonian above would be compressed into a TFIM triangle [1, 2]. The periodic boundary condition term $X_n X_1$ prevents that, and cannot be represented via TFIM blocks. Instead, we provide the following Q -block mapping or this Hamiltonian

$$\begin{aligned} Q^{\text{PTFIM}}(\theta) &= e^{i\theta Z_2 Z_3 \dots Z_n} = e^{i\theta Z_1 P_Z}, \\ B_{2i-1}^{\text{PTFIM}}(\theta) &= e^{i\theta Z_i}, \\ B_{2i}^{\text{PTFIM}}(\theta) &= e^{i\theta X_i X_{i+1}}, \end{aligned} \quad (\text{B2})$$

where the superscript PTFIM stands for periodic transverse field Ising model, and $P_Z = Z_1 Z_2 \dots Z_n$ is the Z -parity operator.

Each term in the Hamiltonian can be represented via the mapping above. As it can be seen, apart from the boundary term $X_n X_1$, all other terms are already present in B_i^{PTFIM} . The boundary term can be written as the following:

$$X_n X_1 = -(Y_1 Z_2 \dots Z_{n-1} Y_n) P_Z. \quad (\text{B3})$$

After staring at it enough, one can recognize $Y_1 Z_2 \dots Z_{n-1} Y_n$ as a mixture of hopping and pair creation/annihilation term between sites 1 and n . From the results we obtained from fermionic swap operation, we know that this term can be written as a product of TFIM blocks. Considering that P_Z commutes with all TFIM blocks, we find the following

$$\begin{aligned} X_n X_1 &= -\mathcal{F}_{n-1,n} \dots \mathcal{F}_{2,3} Y_1 Y_2 \mathcal{F}_{2,3}^\dagger \dots \mathcal{F}_{n-1,n}^\dagger P_Z \\ &= -\mathcal{F}_{n-1,n} \dots \mathcal{F}_{2,3} Y_1 Y_2 P_Z \mathcal{F}_{2,3}^\dagger \dots \mathcal{F}_{n-1,n}^\dagger \\ &= \mathcal{F}_{n-1,n} \dots \mathcal{F}_{2,3} e^{i\frac{\pi}{4} Z_1} e^{i\frac{\pi}{4} Z_2} X_1 X_2 P_Z e^{-i\frac{\pi}{4} Z_2} e^{-i\frac{\pi}{4} Z_1} \mathcal{F}_{2,3}^\dagger \dots \mathcal{F}_{n-1,n}^\dagger, \end{aligned} \quad (\text{B4})$$

which is a product of the TFIM blocks and $Z_1 X_2 P_Z$. This new gate can be written as the following

$$X_1 X_2 P_Z = e^{i\frac{\pi}{4} Z_1} e^{i\frac{\pi}{4} X_1 X_2} Z_1 P_Z e^{-i\frac{\pi}{4} X_1 X_2} e^{-i\frac{\pi}{4} Z_1}. \quad (\text{B5})$$

Thus, a rotation with the periodic boundary term $X_1 X_2$ can be written via the TFIM blocks, and rotation with $Z_1 P_Z$ which is Q^{PTFIM} itself.

Let us show that the mapping Eq. (B2) is a Q -block mapping. Since $B_i^{\text{PTFIM}} = B_i^{\text{TFIM}}$, we know that the block rules are already satisfied [1, 2]. Thus, we only need to show that the Q -block rules are satisfied. The Q -fusion rule is satisfied via the following relation

$$Q^{\text{PTFIM}}(\alpha) Q^{\text{PTFIM}}(\beta) = Q^{\text{PTFIM}}(\alpha + \beta). \quad (\text{B6})$$

Q -commutation is satisfied with B_{2i-1}^{PTFIM} because $[Z_i, Z_1 P_Z] = 0$, and with B_{2i}^{PTFIM} with $i \geq 1$ since $[X_i X_{i+1}, Z_1 P_Z] = [X_i X_{i+1}, Z_2 Z_3 \dots Z_n] = 0$. Finally, as it was the case for the TFIM Q -blockmapping in Eq. (48), Q -turnover property of the PTFIM mapping follows from the Euler decomposition of the following $\mathfrak{su}(2)$ generated by $Z_1 P_Z$ and $X_1 X_2$:

$$\mathfrak{su}(2) \equiv \text{ispan}\{Z_1 P_Z, X_1 X_2, Y_1 X_2 P_Z\}. \quad (\text{B7})$$

Therefore, via Thm. 1, time evolution of the Hamiltonian in Eq. (B1) can be compressed to a diamond.

In this form, the compression will lead to a circuit with n qubits with $\mathcal{O}(n^2)$ depth and $\mathcal{O}(n^2)$ CNOT gates, due to the fact that $Q^{\text{PTFIM}}(\theta)$ require $2n-4$ CNOTs and the same depth. With the observation $P_Z = Z_1 Z_2 \dots Z_n$ commuting with every B_i^{PTFIM} and Q^{PTFIM} , one can add one more qubit and reduce the circuit complexity into $\mathcal{O}(n)$ depth and $\mathcal{O}(n^2)$. To do so, one should put the Z -parity information into the added ancilla qubit, and apply controlled evolution via the ancilla by replacing $Q^{\text{PTFIM}}(\theta)$ with

$$Q^{\text{TFIM}}(\theta) = e^{i\theta Z_0 Z_1} \quad (\text{B8})$$

where 0 is the ancilla qubit. This is the Q -block we have introduced in Eq. (43).

2. TFX Y Model with Periodic Boundary Condition

Consider the following TFX Y Hamiltonian with periodic boundary condition

$$\mathcal{H}(t) = \sum_{i=1}^n \left(\tilde{J}_i(t) X_i X_{i+1} + \tilde{K}_i(t) Y_i Y_{i+1} \right) + \sum_{i=1}^n \tilde{h}_i(t) Z_i \quad (\text{B9})$$

where $X_{n+1} := X_1$ and $Y_{n+1} := Y_1$. We know that if it was not periodic but open boundary condition, the evolution under the Hamiltonian above would be compressed into a TFIM triangle [1, 2]. Here, we will show that the Q -block mapping given in Eq. (B2) is capable of compressing the evolution of the periodic TFX Y Hamiltonian above.

We already know that the mapping Eq. (B2) is a Q -block mapping. The difference between the TFX Y and the TFIM Hamiltonians is the YY interaction. The following shows that the YY terms can be generated via the terms given in TFIM:

$$Y_i Y_j = e^{i\frac{\pi}{4} Z_i} e^{i\frac{\pi}{4} Z_j} X_i X_j e^{-i\frac{\pi}{4} Z_i} e^{-i\frac{\pi}{4} Z_j}. \quad (\text{B10})$$

In a similar way, we can show that every term in the following “generalized” TFXY model can be generated via the terms in the TFIM Hamiltonian:

$$\begin{aligned} \mathcal{H}(t) = & \sum_{i=1}^n \left(\tilde{J}_i(t) X_i X_{i+1} + \tilde{K}_i(t) X_i X_{i+1} \right. \\ & \left. + \tilde{L}_i(t) X_i Y_{i+1} + \tilde{R}_i(t) Y_i X_{i+1} \right) \\ & + \sum_{i=1}^n \tilde{h}_i(t) Z_i, \end{aligned} \quad (\text{B11})$$

where new XY and YX terms are also added. Since the periodic TFIM terms can be generated via the Q -block mapping Eq. (B2), then every term given in both Hamiltonians Eq. (B9) and Eq. (B11) can be represented via the Q -block mapping Eq. (B2) as well, and their evolution can be compressed into a diamond via Thm. 1. The properties of the resulting fixed depth circuit will be exactly the same as in Appendix B 1.

Appendix C: P -blocks and Controlled Free Fermions

Here, we introduce an new set of rules, referred to as the P -block rules, which enable an efficient compression algorithm, serving as an alternative to the Q -block rules. These rules yield results comparable to those obtained with the Q -block rules discussed in Sec. IV. In this section, we will be explaining the P -block rules, P -block compression, and introduce a P -block mapping for the controlled free fermions without the creation-annihilation operator. We discuss that this P -block mapping can be considered as the TFXY version of the Q -block mapping introduced in Sec. IV B, and has certain pros and cons over the controlled free fermionic Q -block mapping, e.g. P -block mapping can lead to a CNOT efficient circuit without the application of the TFIM \rightarrow TFXY transformation given in Eq. (12), while Q -compression is based on TFIM compression, and can be implemented faster.

1. P -blocks and P -block Compression

We define P -blocks and P -diamonds as follows:

Definition 4 (P -Block). Given blocks B_i with $i \geq 1$, define a “ P -Block” $P = P(\vec{\theta})$ as a structure that satisfies

1. **P -fusion:** For any set of parameters $\vec{\alpha}$ and $\vec{\beta}$, there exist \vec{a} such that

$$P(\vec{\alpha}) P(\vec{\beta}) = P(\vec{a}), \quad (\text{C1})$$

2. **P -commutation:** For any set of parameters $\vec{\alpha}$ and $\vec{\beta}$

$$P(\vec{\alpha}) B_i(\vec{\beta}) = B_i(\vec{\beta}) P(\vec{\alpha}), \quad i > 1, \quad (\text{C2})$$

3. **P -turnover:** For any set of parameters $\vec{\alpha}, \vec{\beta}, \vec{\gamma}$ and $\vec{\theta}$ there exist $\vec{a}, \vec{b}, \vec{c}$ and \vec{d} such that

$$P(\vec{\alpha}) B_1(\vec{\beta}) P(\vec{\gamma}) B_1(\vec{\theta}) = B_1(\vec{a}) P(\vec{b}) B_1(\vec{c}) P(\vec{d}). \quad (\text{C3})$$

If P and blocks B_i satisfy the properties listed above, we will say that $\{P, B_i\}$ is a P -block mapping.

Definition 5 (P -Diamond). Define a “ P -diamond” with height n as

$$D_n(\vec{\alpha}, \vec{\beta}) := \prod_{m=1}^{n+1} \left[\left(\prod_{i=n \downarrow}^1 B_i(\vec{\alpha}_{i,m}) \right) P(\vec{\beta}_m) \right] \quad (\text{C4})$$

where \downarrow in the product means that the multiplication is done in the decreasing order, and B_i are blocks, P is a P -block and each term in the product can have different variables.

An illustration of the P -block rules is given in Fig. S1 panels (a-c), and a P -diamond with height 4 is illustrated in Fig. S1 panel (d). Now we will prove that a P -diamond can absorb any block B_i and a P -block.

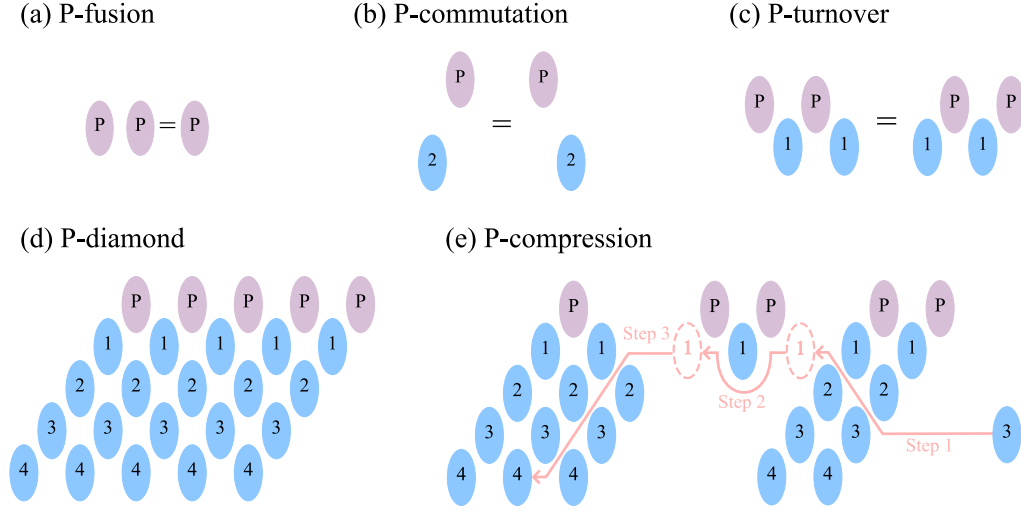


FIG. S1. (a-c) P -block properties given in Def. 4. Notice that the P -turnover is different from both turnover and Q -turnover rules, as it includes 4 blocks rather than 3 blocks. (d) The P -diamond structure defined in Def. 5 with heights $n = 4$. (e) Proof of Thm. 2, i.e. how the P -diamond can absorb a block. For this specific illustration, size of the P -diamond is $n = 4$ and the index of the block is $i = 3$. The block is lifted by other blocks via B -turnover operations, then passes through via P -turnover operation, and gets pushed down via B -turnover operations finally to be absorbed via a B -fusion operation.

Theorem 2 (P -compression). *A P -diamond with height n can be merged with any block B_i with $i = 1, 2, \dots, n$ and P -block P :*

$$\begin{aligned} D_n(\vec{\alpha}, \vec{\beta}) P(\vec{\gamma}) &= D_n(\vec{a}, \vec{b}), \\ D_n(\vec{\alpha}, \vec{\beta}) B_i(\vec{\theta}) &= D_n(\vec{u}, \vec{v}). \end{aligned} \quad (\text{C5})$$

Merging P requires only one P -fusion. Merging B_i requires $n + i - 2$ B -turnovers, 1 P -turnover and 1 B -fusion.

Proof. The proof of this results is given diagrammatically in Fig. S1 panel (e). Since it is trivial to show that the P -diamond structure can absorb a P -block using the P -fusion operation, we only discuss how the P -diamond can absorb B_i . The illustration is for $n = 4$ and $i = 3$ case, but the same mechanism generalizes to arbitrary (finite) system sizes and B_i .

In step 1, the block B_i gets shifted upwards through the P -diamond via normal block turnover operations until its index reaches 1. Starting at index i (which is 3 in the figure above), this upward movement requires $i - 1$ turnover operations. In step 2 a P -turnover is applied, which brings the block from the right side to the left side of the formation of blocks shown in the middle of the figure above. Finally, in step 3, we can shift the block downward to the final row of blocks in the P -diamond. This again requires only normal block turnover operations, more precisely, we need $n - 1$ turnover operations to move the block down to the bottom row of a P -diamond of height n ($n = 4$ in the figure above). At this stage, the block can then be fused with corresponding index n block. This operation requires $n + i - 2$ turnover operations, 1 P -turnover operation and 1 B -fusion operation in total. \square

In the next section we discuss controlled free fermionic Hamiltonians as an example of a P -compressible Hamiltonian. However, we note that the theorem does not directly rely on the Hamiltonian, it only requires a set of circuit elements that follow the B -block and P -block rules. Thus, any circuit that is solely composed of gates that satisfy these rules can be compressed to a P -diamond, whether it is a controlled time evolution circuit of a free fermionic system or not.

2. P -block mapping for Controlled Free Fermions

In Sec. IV B, we provided a Q -block mapping for controlled free fermionic Hamiltonian given in Eq. (42), and proved that the TFIM blocks and the gate $e^{i\theta Z_0 Z_1}$ was sufficient to represent time evolution of controlled free fermions. Here, we will show that the gate $e^{i\theta Z_0 Z_1}$ satisfies P -block rules if we consider a TFX block mapping given in Fig. 1(g) and

Eq. (10), i.e. we will show that the following is a P -block mapping:

$$\begin{aligned} P^{\text{TFXY}}(\theta) &= e^{i\theta Z_0 Z_1}, \\ B_i^{\text{TFXY}}(\vec{\theta}) &= e^{i\theta_1 Z_i} e^{i\theta_2 Z_{i+1}} e^{i\theta_3 X_i X_{i+1}} e^{i\theta_4 Y_i Y_{i+1}} e^{i\theta_5 Z_i} e^{i\theta_6 Z_{i+1}}. \end{aligned} \quad (\text{C6})$$

The P^{TFXY} satisfies the P -fusion due to the following:

$$P^{\text{TFXY}}(\alpha) P^{\text{TFXY}}(\beta) = P^{\text{TFXY}}(\alpha + \beta). \quad (\text{C7})$$

P -commutation is satisfied because for any $i > 1$, P^{TFXY} and B_i^{TFXY} act on different sets of qubits.

The left-hand side of the P -turnover equation with the P -block mapping Eq. (C6) can be rewritten in terms of TFIM elements by transforming the TFX block (i.e. a free fermionic matchgate) into TFIM elements by using the transformation given in Eq. (13). The entire expression can then be written as a sequence of Q^{TFIM} , B_1^{TFIM} , B_2^{TFIM} , and B_3^{TFIM} . Thus, it can be compressed into a Q -diamond represented by the mapping given in Eq. (43). Applying the grouping given in Fig. 7(e) to this Q -diamond yields the right-hand side of the P -turnover equation, proving that the P -turnover equality is satisfied in one direction. We can prove it in the other direction by simply observing the symmetry of the Q -block mapping rules, and applying the above procedure in reverse, i.e., compressing to a reverse Q -diamond. Thus, the mapping Eq. (C6) satisfies the P -turnover property as well, and is a P -block mapping.

The P -block mapping given in Eq. (C6) has its advantages and disadvantages over the Q -block mapping for the controlled free fermions given in Eq. (43). By using this P -block mapping, one can compress the controlled free fermionic evolution simply by using the TFX blocks, and TFX block rules given in [1, 2], and can obtain a CNOT efficient circuit without the application of the TFIM \leftrightarrow TFX transformations given in Eqs. (12) and (13). Thus, for devices that uses CNOT gates, it is more natural to use matchgates i.e. the TFX blocks, and P^{TFXY} directly to implement the compression for the controlled free fermionic evolution. However, the Q -block mapping turns out to be more fundamental as the TFIM mapping, and faster to implement compression. In addition, Q -blocks can be generalized to controlled free fermions with creation as given in Sec. IV C.